Explanation of Water Distribution Variations in the Landfill Using Electrical Resistivity Tomography

Zhenlu Ren

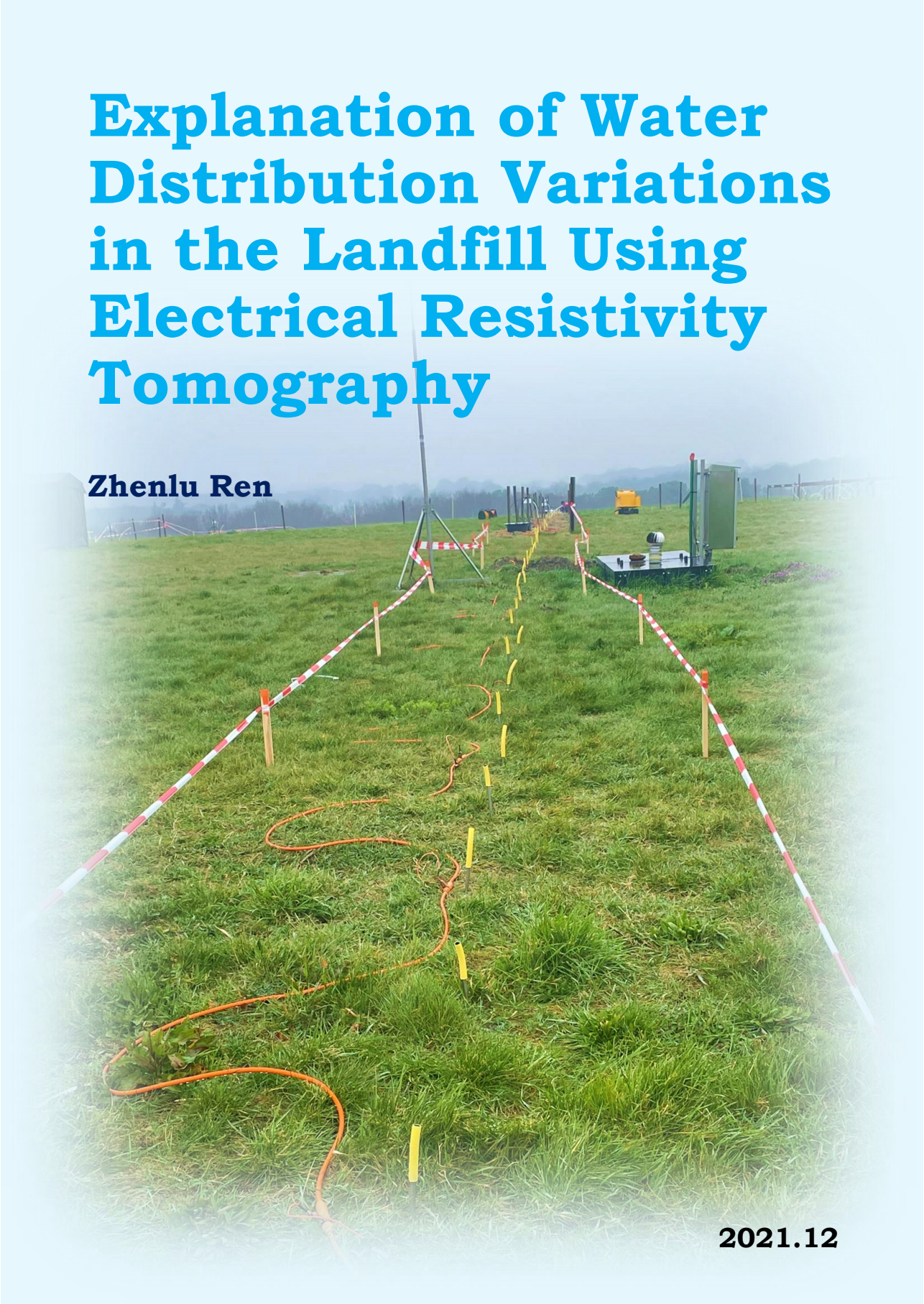

2021.12

Explanation of Water Distribution variations in the Landfill Using Electrical Resistivity Tomography

Zhenlu Ren

Explanation of Water Distribution variations in the Landfill Using Electrical Resistivity Tomography

by

Zhenlu Ren

in partial fulfillment of the requirements for the degree of

Master of Science

in civil engineering

at the Delft University of Technology

to be defended publicly on Wednesday December 16th 2021 at 9.00 AM.

Student name:	Zhenlu Ren	
Student number:	5008468	
Supervisor:	Prof. Dr. Ir. T. J. Heimovaara,	TU Delft
Thesis committee:	Dr. J. Gebert,	TU Delft
	Dr. Ir. D. S. Draganov,	TU Delft

TU Delft Delft University of Technology

CURE

Contents

Acknowledgements

This research is funded by the 'CURE' project, I really appreciate Prof. dr. ir. Timo Heimovaara for providing me this precious research opportunity and for giving me numerous support and guidance. Besides, I would like to thank Juan Chavez Olalla, who inspired me to solve many problems in the process of designing experiments, doing fieldwork and analyzing data. During the ERT measurement campaign, all the people in our research group, especially Liang Wang and Roland Klasen, and in Attero company gave me plenty of supports and guidance, without them, I would not be able to carry out such large field work with so many heavy machines.

The task of writing this dissertation is huge, I gratefully acknowledge my supervisor Prof. dr. ir. Timo Heimovaara and my thesis committee for reviewing my work and giving me innumerable constructive suggestions.

At last, many hanks to my friends in Netherlands and in China for accompanying me through this special time. Many thanks to my father, who gives me countless spiritual encouragement and material support, and to my mother, who gave me the courage to face life.

Summary

The continuous accumulation of solid waste has posed a great threat to the environment of our future generations. A novel approach that is currently under development is to treat the waste collected in an engineered landfill in order to reduce the emission potential to an environmentally acceptable level. The main topic for this research is to improve the understanding of how leachate is distributed throughout the landfill Kragge and how this distribution varies in time. This is important for identifying the long-term behavior of the landfill and for managing landfill waste.

At the start of this project, we have a number of water level measurements obtained from various wells in the landfill. Straightforward spatial interpolation of this data leads to unexpected results. Most likely this is caused by the highly complex heterogeneity in this porous system. For this reason, this research aims to apply Electrical Resistivity Tomography (ERT) technology to explain the water distribution variations between wells. The apparent resistivity along several lines are measured over depth using different arrays. Some scripts written in Python with 'pyBERT' and 'pyGIMLi' packages are used to get electrical resistivity inversion results from the apparent resistivity. It is known that the decrease in the water content leads to a significant increase in the resistivity. Therefore, the possible existence of saturated and unsaturated blocks in the waste body can be visualized from the inversion maps.

Initially, the interface between the saturated and unsaturated zones is expected to be identified from Laplacian edge detection, while the results indicate that this technique fails to represent the area boundaries under highly-heterogeneous situations. Subsequently, Archie's law and van Genuchten equation are coupled to give a relation between the resistivity and water pressure head. Archie's law is used to compute the resistivity from water content and van Genuchten equation is used to compute the water content

from the water pressure head. There are two hypotheses during this analysis: (a) where the resistivity is $20\Omega \cdot m$ gives the interface of dry and wet zones; and (b) the landfill leachate is under hydrostatic condition. Then the water pressure head is the distance from the interface, which can be read from the inversion maps. By selecting a certain range of empirical parameters, the computed resistivity−pressure head curves provide relatively good fits to the measured results.

List of Figures

List of Tables

1

Introduction

1.1. Research background

Landfills are created by dumping municipal Solid Waste (MSW) discarded by the public in their daily lives. The behavior of the landfill is controlled by physical and bio-geochemical processes (Rodrigo-Ilarri *et al.*, 2020). Rainfall infiltrates through the cover layer and is stored in the voids of the waste body where it competes for space with gas (mainly CO_2 and CH_4). A fraction of the solid material present in the waste body (both organic and inorganic) dissolves into the water and leaches toward the drainage system where it forms leachate. Two of the most challenging solutes for long-term aftercare are chloride (Cl^-) and ammonium (NH^{4+}). As leachate potentially contains a wide range of toxic solute mass, it may result in extremely negative effects on surface water and groundwater quality if directly released into the environment (Kjeldsen *et al.*, 2002).

The traditional method to reduce the emission potential is to isolate the waste from the environment. An impermeable geo-membrane is laid at the bottom before constructing the drainage system to prevent the outflow of the leachate. A watertight cover is installed above the system once the landfill is

filled so that the rainfall and oxygen (O_2) stop entering. However, this requires eternal care of the cover, since the possible broken may restart the leakage of leachate.

To accelerate the degradation and reduce the aftercare efforts, the new concept is to improve the leachate quality by active treatment of the waste body using infiltration and recirculation of leachate and / or aeration (Kattenberg and Heimovaara, 2011). Full-scale in-situ experiments have been performed in three pilot landfills (Braambergen, Wieringermeer, and Kragge) in the Netherlands for years, to investigate whether the sustainable aftercare methods can effectively reduce the remaining emission potential to an environmental-acceptable level (Kattenberg and Heimovaara, 2011). Field observation indicates the high heterogeneity of water distribution: some areas have been completely saturated, dissipating slowly over time, some steep gradients occur in the water levels between adjacent wells. Most striking was that relatively dry waste was found to occur below fully saturated waste, during drilling new boreholes, fresh excavated waste appeared to range from completely dry to fully saturated (Chapter 2).

This research serves as part of the work in the project "Coupled mUlti-process research for Reducing landfill Emissions" (CURE). The aim is to identify, describe and predict the coupled bio-geochemical process of the landfills and verify that the emission potential of contaminations will be reduced to a permissible range (https://www.nwo.nl/en/projects/ocenwgroot2019092). Kragge is one of the pilot landfills of the project, where the wastes are biologically and bio-geochemically stabilized by infiltration and leachate recirculation.

1.2. Landfill hydrology model

A classic water balance model to predict the amount of leachate is called Hydrological Evaluation of Landfill Performance (HELP) (Schroeder *et al.*, 1994). It is a quasi-two-dimensional hydrologic model, calculating the leachate discharge as the difference between landfill precipitation and the sum of evaporation, runoff, infiltration as well as water storage (Schroeder *et al.*, 1994). However, the model cannot predict the long-term leachate discharge

rate with high accuracy because the water flow processes inside the landfill are not considered (Fellner and Brunner, 2010).

Further research shows that the flow of water through landfills is highly non-uniform and dominated by preferential pathway (Fellner, 2004, Rosqvist and Bendz, 1999, Rosqvist *et al.*, 2005), which leads to the inconsistency between simulated leachate generation and the field measurements in the previous models (Fellner and Brunner, 2010). The landfill matrix domain is characterized by low permeability and high retention capacity (Fellner and Brunner, 2010). Water storage and flow mainly in horizontal layer because of the horizontal "barriers", vertical flow channels cause a limited fast flow in the vertical direction (Fellner and Brunner, 2010). The model distinguishes the channel domain with high hydraulic conductivity and the slow-flow matrix domain with high water retention capacity (Fellner and Brunner, 2010). However, since the non-uniformity of the water distribution is set by model parameters, this model cannot infer the degree of the water flow heterogeneity (Rosqvist *et al.*, 2005).

The model that used in the CURE project is based on mass balances of water to estimate the changes in water content in the landfills (van Turnhout, 2017). The water balance is based on the divergence of the fluxes in the landfill system. The landfill is modelled with cover layer, waste body and drainage system (Figure 1.1). The input data are the daily rainfall and evaporation downloaded from the Royal Dutch Meteorological Institute (KNMI), and the output results are the simulated leachate quantity in the drainage system. Part of the water infiltrates from the cover layer to the waste body and the remaining part is stored in the cover layer. Considering the high heterogeneity, the flow through the waste body is described in a probabilistic Lagrangian modelling approach, with a stochastic travel time distribution. The time series of daily infiltration rates from the cover layer is convoluted with a stochastic travel time distribution, indicating how long it takes for each water drop infiltrating to reach the point of outflow (Hrachowitz *et al.*, 2016, Zacharof and Butler, 2004). The model parameter to describe the initial states is the emission potential, therefore, the water content distribution in the landfill remains an essential part to assess the leachate (van Turnhout, 2017, Heimovaara *et al.*, 2015).

1

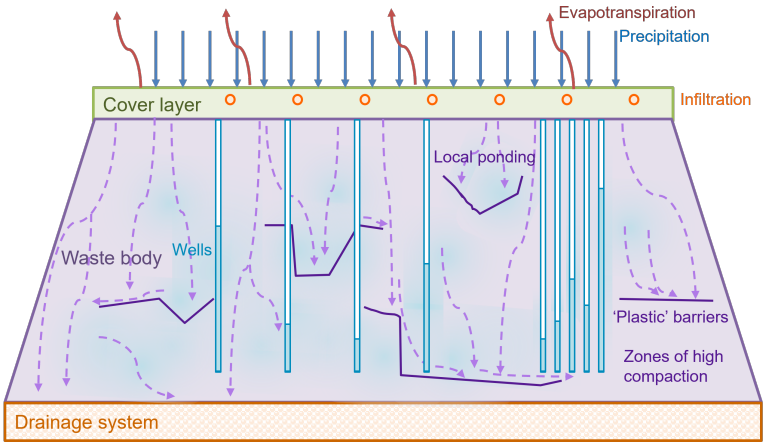

Figure 1.1: Sketch of the landfill hydraulic model.

1.3. Dissertation outline

This thesis starts with the introduction of emission potential problems in the traditional and novel types of filling waste in the landfill and the physical processes in the waste body (Chapter 1). Then the current status of the landfill and the analysis of water level in the wells are described in Chapter 2. The research questions are proposed in Chapter 3. In Chapter 4, some representative application cases of applying ERT in the landfill are summarized. Chapter 5 illustrates the basic theory of ERT measurement and inversion. Chapter 6 describes the arrangements of field experiments and analytical methods of the measured ERT results. Chapter 7 presents the results of ERT error assessment and apparent resistivity inversion maps. The Laplacian edge detection maps and the resistivity–water pressure head curves are also plotted. Chapter 8 discusses the inversion regularization parameters and further analysis of the parameter selections when fitting the water retention curves. The saturated areas and volumes are estimated. And finally, the conclusions of the thesis are in Chapter 9.

2

Preliminary study

2.1. Landfill status description

The landfill to be considered in this research is De Kragge II, and its top view is shown in Figure 2.1. From bottom to top, the landfill was constructed with the drainage layer, the waste layer and the cover layer. The elevations of the base layer and the top surface are approximately 6.5m and 28m above Normaal Amsterdams Peil (NAP) respectively. The drainage system is filled with sand and its cross section is presented in Figure 2.2. The top layer is covered with vegetation, absorbing the rainfall and producing evaporation. The landfill has been divided into four compartments by 2-meter-high dikes. Cell 1, cell 2 and a small part of cell 3 have covered with an impermeable cover layer. In cell 3 and cell 4, the waste body is treated with leachate infiltration followed by aeration (van Turnhout *et al.*, 2018).

Various wells were installed in the landfill, an overview of the location of the wells in the landfill cell 3 is given in Figure 2.3. The distance between every two gas wells is more than $50m$. Twelve ERT wells are positioned in a three-by-four grid, with the distance around $20m$-$25m$. Besides, two rows of piezometer wells ($P1.$ and $P2.$) were arranged with a space of about $18m$, and

2

the distance between two adjacent piezometer wells is only 0.5m (Figure 2.4). The bottom of the gas wells and ERT wells are basically at the same depth (15m from the landfill surface) (Figure 2.5), which means that those water level were monitored at the similar level, while the depth of the piezometer well filters range from 3m to 13m. Some wells were placed at the slope, therefore there are difference between gas wells top elevation. Some gas wells have deviations in the depth, which were be caused by subsidence, collapse or blockage.

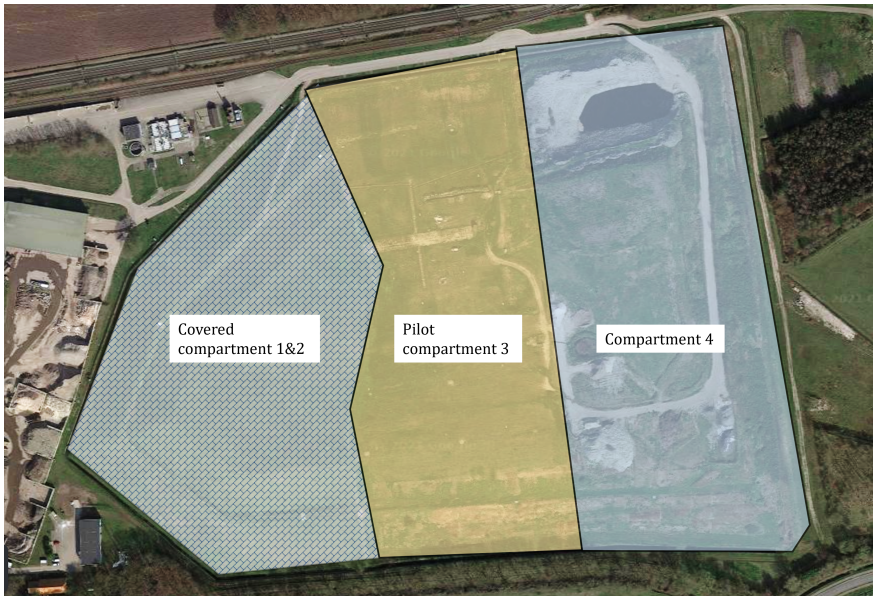

Figure 2.1: Top view of the landfill De Kragge II (The map was captured from Google Earth, 2021).

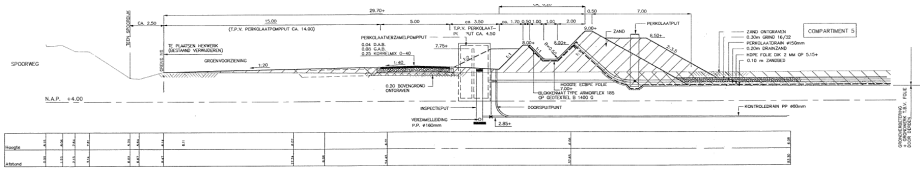

Figure 2.2: Cross section of the base layer (source from the technical report)

Figure 2.3: Photo of Wells site plan in the landfill Kragge.

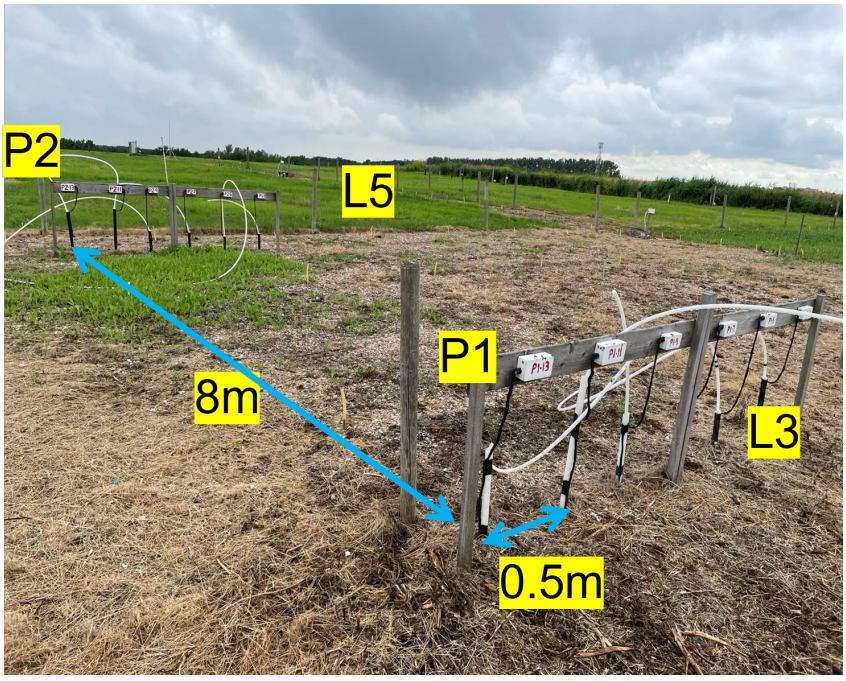

Figure 2.4: Photo of piezometer wells in the site.

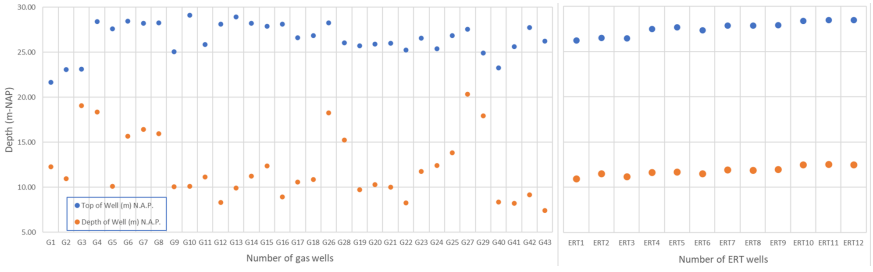

Figure 2.5: Top and bottom depth (in $m - NAP$) of gas wells and ERT wells (well numbers are shown in Figure 2.3).

2.2. Wells water level investigation

The water level data from the wells were investigated to get a primary idea of the hydrological situation of the landfill. The data were recorded on a regular basis, to understand the temporal dynamics of the results, the water level changes over time were plotted (Figure 2.6). These water level data were firstly normalized based on the same vertical datum, to ensure the effectiveness of the comparison. The elevation of the wellheads were measured relative to NAP, and the water level were dipped from the wellheads. Therefore, the water level with reference to NAP can be calculated by Equation 2.1:

$$WL_{NAP} = WH_{NAP} - WL_{top} \tag{2.1}$$

Where WL_{NAP} is the water level calculated from NAP, WH_{NAP} is the elevation of wellheads from NAP, and WL_{top} is the water level from the wellheads.

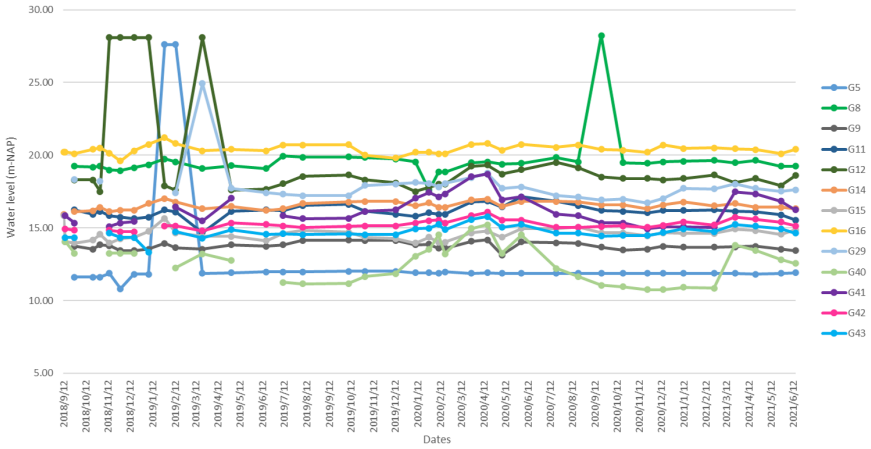

Figure 2.6: Gas well water levels versus time (well numbers are shown in Figure 2.3).

On the other hand, two-dimensional landfill water level spatial distribution maps were interpolated by adopting the Inverse Distance Weighted (IDW) method in QGIS. The values of water level between wells were resorted to the inverse distance to each known water level point (Setianto and Triandini, 2013). The results are shown in Figure 2.7. The blue dots in the figures are

ERT wells with water level data; purple dots are gas wells with water level data; and Red dots are gas wells which were omitted during interpolation.

(a) Gas well water level map in 2021 March 24

(b) Gas wells water level map in 2021 May 26

(c) Gas wells and ERT wells water level map in 2021 March 24

(d) Gas wells and ERT wells water level map in 2021 May 26

Figure 2.7: 2D gas wells and ERT wells water level maps in the landfill De Kragge II, interpolated by IDW method in QGIS.

Furthermore, Figure 2.8 depicts the water level in the piezometer wells measured in 2021 May 18. The grey columns are the area where water was not appeared. The top and bottom of the blue columns represent the surface of the water presented in the wells and the corresponding bottom of the wells as detected by the dip meter respectively. Well $P2.9$ seems to be ruined, therefore no data was recorded.

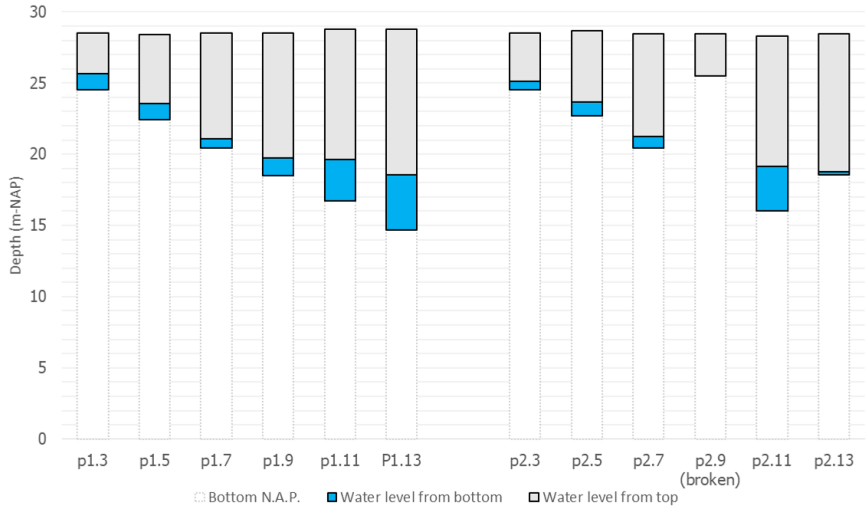

Figure 2.8: Water level from the top and the bottom of piezometer wells.

2.3. Results interpretation

Figure 2.6 indicates that although several wells experienced large fluctuations on individual dates, the water levels remained unchanged during the measurements period (September 2018–June 2021). Therefore, despite the fact that the water level measurement time of gas wells and ERT wells were different, and the measurement dates of ERT wells were limited, the water level in gas wells and ERT wells can still be interpolated in the same map.

Figure 2.7(a) and Figure 2.7(b) show that while the time variability of wells water level are narrow, the spatial variations of water level distribution are non-negligible. It seems that the water levels in the middle of the landfill were high (red areas in the maps), then became lower when approaching the slopes. However, when ERT wells, which spaced relatively closer to each other, were also included, the maps showed more significant fluctuations (Figure 2.7(c) and Figure 2.7(d)) . In addition, field measurements indicate that some wells have been damaged, which further reduces the data that can be obtained from the wells. Therefore, the current number of wells is not sufficient to directly explain the water level distribution in this landfill. On top of that, the contour lines of the water level in the maps form the clear circle around the wells, which are clearly

distinguished from the results in areas without data from wells. This implies that the IDW interpolation method is not applicable in this highly heterogeneous waste body.

Besides, the water level in the piezometer well nests reveals that the distribution of water level is highly variable in even a small zone (Figure 2.8). Field observations also showed that during the drilling of new wells (in 2020 November 26), the collected samples changed from dry to wet at the beginning, then dried out again when going deeper. Therefore, the inference is that there were dry waste areas existing below the saturated zones.

In a word, considering the large distances between wells as well as the extreme discontinuity of observation results, the water table distributions drawing only from the wells data are far from precise, and the understanding that can be obtained is quite limited. Therefore, a geophysical method named Electrical Resistivity Tomography (ERT) was applied, in order to obtain a continuous spatial pattern of the water distribution in the landfill.

3

Research questions

This research aims to verify the water distribution in the landfill. One hypothesis is that the water in the landfill waste body is dominated by preferential flow (Rosqvist *et al.*, 2005). It is believed to be the consequence of the structure of the waste body, in which the presence of plastics leading to large anisotropy in permeability. Water flow in the waste body is assumed to occur along primarily horizontal flow paths, which intersect a limited number of vertical flow paths (which could be vertical gas wells) (Fellner and Brunner, 2010). Therefore, the water in the waste body is discrete and cannot form continuous water table.

Using the water level measured in the wells, 2D water table distribution maps can be derived. The number of wells, however, is inadequate considering the total surface of the landfill cell, as a result, the spatial distribution of water is difficult to interpolate and the storage in the unsaturated zone is difficult to quantify. Electrical Resistivity Tomography (ERT) is a non-intrusive geophysical technique that can be used to obtain information about the properties of the waste body in depth. In this project, ERT is applied to analyze the spatial water distribution, to have a better understanding of the variation in the water content in the waste body. Changes of resistivity from ERT results are correlated to the

information from wells and infiltration lines.

Therefore, the research questions are:

1. Can the water distribution in the landfill De Kragge (cell 3) be visualized by the electrical resistivity inversion maps?
2. How does the spatial distribution of water table in the landfill De Kragge (cell 3) look like?
   (a) Are there any steep gradients in the spatial distribution of the water table?
   (b) Are there any unsaturated bulk present under the saturated zones?
   (c) Can the ERT results be used to explain the water levels in the wells?
3. Can the variations in the water content in the waste body be linked to variations of the resistivities from ERT results?

4

Literature review

Electrical resistivity tomography (ERT) is a geophysical method in which electrical currents are injected between two electrodes on the subsurface and voltages are measured on another two electrodes. These measurements are used to calculate soil resistivity maps (Zhou and Kanl, 2018). ERT has been shown to be an affordable, non-invasive, and rapid technique for generating large-scale spatial models of subsurface physical parameters (Brunet *et al.*, 2010, Neyamadpour, 2019). It can produce information at a lower cost than conventional methods because of its high efficiency and short operation time.

Since 1980s, ERT have been applied widely to visualize the water distribution in a field scale (Brunet *et al.*, 2010, Topp *et al.*, 1980, Kuras *et al.*, 2009, Clément *et al.*, 2010, Chrétien *et al.*, 2014). It has been shown that the presence of water reduces bulk resistivity (Archie, 1942, Audebert *et al.*, 2016), so the resistivity changes can be attributed to changes in water content (de Jong *et al.*, 2020). Furthermore, time-lapse ERT can be used to monitor the leachate recirculation and water level changes in the waste (Audebert *et al.*, 2016, 2014, Clément *et al.*, 2011). By comparing ERT images with experimental injected volumes, it was shown that time-lapse ERT can (a) precisely locate the injection plume, (b) delineating its depth and lateral extension; and (c) be used to

estimate some hydraulic properties of the waste (Clément *et al.*, 2011).

Some attempts have been made to find a mathematical relationship between resistivity and water content. For example, Archie's equation can give a relationship between resistivity and water content (Archie, 1942). The parameters in the equation need to be estimated in the laboratory. The feasibility has been verified in some cases, such as monitoring the soil water content on a dike model (Rings *et al.*, 2008). In this case, the resistivity values were obtained from ERT inversion maps. External geo-physical methods can be of significant advantage to obtain more reliable ERT time-lapse result (Clément *et al.*, 2011), so time-domain reflectometry (TDR) was also applied to provide a suitable calibrated resistivity-saturation relationship (Rings *et al.*, 2008). Another case study gave a correlation between electrical resistivity and volumetric water content with 3D ERT monitoring in a landfill. The correlation was concluded by comparing the laboratory measurements and field survey (Neyamadpour, 2019). As seen from these two examples, the relationship is empirical and not universal, which makes it impossible to quantify the water content from the field electrical resistivity value using the same resistivity-saturation relation.

In fact, the above methods have a fundamental problem due to the ERT data interpretation is based on the inversion process (Audebert *et al.*, 2014). The measurement of electrical resistivity is accurate, while the inversion results may not be true, so the resistivity-saturation relationship obtained may not be accurate. These reasons include: (a) it is difficult to choose appropriate inversion parameters (Audebert *et al.*, 2014); (b) wrong changes of resistivity can be calculated (Clément *et al.*, 2010); and (c) it is difficult to delineate the infiltration and recirculation front based on resistivity models because of the smoothness of the inversion results (Audebert *et al.*, 2014).

To solve those problems, a new method called multiple inversions and clustering strategy (MICS) is proposed by Audebert *et al.* (2016, 2014). The results demonstrated that this strategy could improve the delineation of the infiltration front, but the impact of other parameters such as the electrode spacing unit and the geoelectrical array used for forward calculation were not considered to build the resistivity model (Audebert *et al.*, 2014). Chavez Olalla

(2017) presented a systematic protocol to find an optimum survey strategy, which is a balance between resolution, covered area, acquisition time, and data error. With this strategy, high resolution ERT information can be retrieved while covering the largest possible area, but this method has not been verified.

In general, the most common way to analysis the ERT results is to correlate the volumetric water content to resistivity by Archie's law, while the parameters are always chosen from experience, for example, Grellier *et al.* (2007) tested several sets of parameters, the results can have good fits with measured data, while extra lab experiments are required to measure the water content. Besides, Laplacian edge detection technique has been proved to be effective in detecting layered soil from geophysical tomography (Hsu *et al.*, 2010, Chambers *et al.*, 2012, Chavez Olalla *et al.*, 2021). Although material properties and interfaces derived from tomography are not always accurate, it can be assumed that they preserve information about the trend of variability of the subsurface (Chavez Olalla *et al.*, 2021). This has not been applied in the landfill, therefore, this study also tried estimate the interface of saturated and unsaturated zones using this method.

5

ERT Theory

5.1. ERT basic Theory

Electrical Resistivity Tomography (ERT) is a direct current (DC) resistivity method that has been widely applied to investigate near-surface physical proprieties. The obtained resistivity distribution can represent the differences of mineralogy, porosity and the water content (Samouëlian *et al.*, 2005). In this section, the basic relationships behind the ERT is presented based on the work done by Dey and Morrison (Dey and Morrison, 1979, Loke, 2013).

The fundamental theory of ERT is Ohm's law. The current density (J) in a continuous medium is give in vector form:

$$J = \sigma E \tag{5.1}$$

in this equation, σ is the isotropic medium conductivity, which is the reciprocal of the medium resistivity (ρ):

$$\sigma = \frac{1}{\rho} \tag{5.2}$$

E is the electric field intensity, which is the negative gradient of electric potential (ϕ):

$$E = -\nabla\phi \tag{5.3}$$

therefore, the current density can be expressed as:

$$J = -\frac{1}{\rho}\nabla\phi \tag{5.4}$$

Electrical resistivity survey uses electrodes to inject the current, which is induced by giving a fixed voltage from the ERT device. The error introduced by not considering the size of electrodes is negligible compared to the total boundary area and inevitable modelling errors (Hanke *et al.*, 2011), so the electrodes can be simplified as point sources. In practice, one ERT measurement requires two electrodes to induce the current ($C1$ and $C2$) and another two electrodes to measure the potential / voltage ($P1$ and $P2$) (Figure 5.1, where A, B are the current injection electrodes and M, N are the potential receiving electrodes). For a single point in a homogeneous half-space, the current moves radially away from the source and the potential varies inversely with distance from the current source. The equipotential surface is hemispherical and perpendicular to the current path. The expression of ideal single point potential is:

$$\phi = \frac{\rho I}{2\pi r} \tag{5.5}$$

where r is the distance from a calculated point to the current source. Then the potential between the electrode pair $C1$ and $C2$ can be calculated by:

$$\phi = \frac{\rho I}{2\pi}\left(\frac{1}{r_{C1}} - \frac{1}{r_{C2}}\right) \tag{5.6}$$

where r_{C1} and r_{C2} are the distance from the calculated point to the two injection points $C1$ and $C2$ respectively. Finally, in the quadrupole condition, the theoretical solution of potential difference between the electrodes $P1$ and $P2$ becomes:

$$\Delta\phi = \phi_1 - \phi_2 = \frac{\rho I}{2\pi}\left(\frac{1}{r_{C1P1}} - \frac{1}{r_{C2P1}} - \frac{1}{r_{C1P2}} + \frac{1}{r_{C2P2}}\right) \tag{5.7}$$

where r_{CiPi} $(i = 1, 2)$ is the distance between injection point Ci and measurement point Pi.

The resistivity term can be derived from Equation 5.7:

$$\rho_a = k\frac{\Delta\phi}{I} \tag{5.8}$$

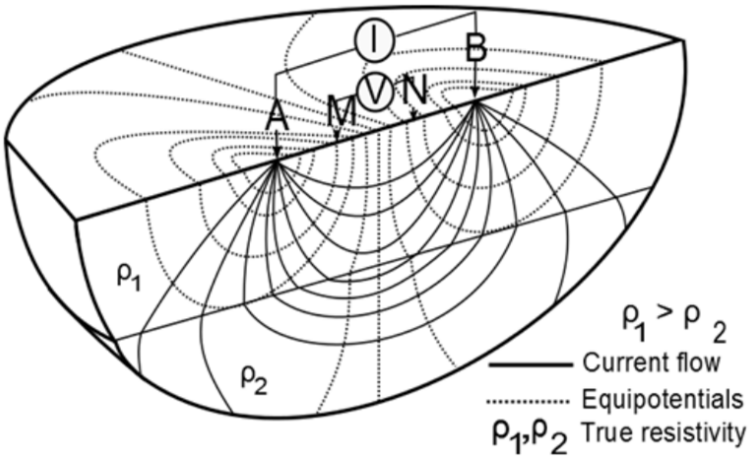

Figure 5.1: Schematic diagram of the potential distribution in a two-layer homogeneous half-space (Source from Knödel *et al.* (1997), Wiekenkamp (2012)).

in which k is the geometric factor:

$$k = \frac{2\pi}{\left(\frac{1}{r_{C1P1}} - \frac{1}{r_{C2P1}} - \frac{1}{r_{C1P2}} + \frac{1}{r_{C2P2}}\right)} \tag{5.9}$$

and the resistance that describe the magnitude of which the substance impedes the flow of current is calculated by:

$$R = \frac{\Delta\phi}{I} \tag{5.10}$$

Since the current generation and voltage measurement are not at the same electrode pair, the obtained resistance is an average value through the current flow path. Assuming the homogeneous ground situation gives the same resistance value under the same electrode arrangement. However, the actual current always goes 3D in the heterogeneous subsurface that the resistance values differ locally. Therefore, Equation 5.8 calculates the 'apparent' resistivity (ρ_a) instead of the 'true' resistivity (ρ).

5.2. ERT measurement Theory

To begin with, the concept of 'array' is introduced, which means the geometrical configuration of the four electrodes that are used to inject current and receive voltage. In order to measure the resistivities along a line over depth, multiple electrode combinations are required. The most commonly used arrays for the landfill waste body measurement are dipole-dipole array and Wenner-Schlumberger array. In the dipole-dipole array, two electrodes to induce current ($C1$ and $C2$) and the electrodes to measure voltage ($P1$ and $P2$) are distributed on two sides for each measurement. The spaces between $C1 - C2$ and $P1 - P2$ are the same, while the distance between $C2$ and $P1$ increase with the increase of array level. Wenner-alpha array can be seen as a special case for Schlumberger array. The two outer electrodes are the current source electrodes ($C1$ and $C2$), and the inner two electrodes are the potential receiving electrodes ($P1$ and $P2$). With the increase of array level, the spaces between four electrodes ($C1 - P1$, $P1 - P2$, $P2 - C2$) increase by the same multiple in the Wenner-alpha array, while in the Schlumberger array, only the spaces between electrodes $C1 - P1$ and $P2 - C2$ increase.

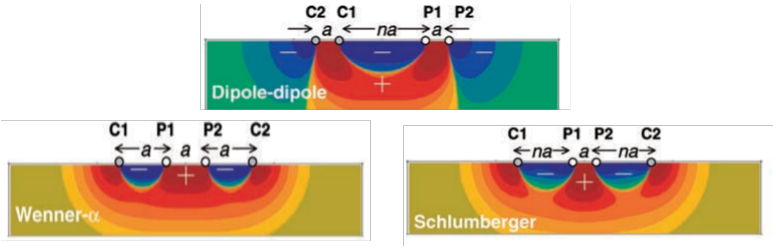

Figure 5.2: Sensitivity distributions for different electrode arrays (Dahlin and Zhou, 2004).

The array type has a large influence on the sensitivity of the electrical resistivity measurements (Wiekenkamp, 2012). Figure 5.2 gives a schematic diagram of how the electrodes are arranged under different array types, it also gives the sensitivity patterns of different arrays for 2D resistivity surveys (Dahlin and Zhou, 2004). It indicates that the dipole-dipole array is good at detecting horizontal changes, namely it is good at mapping vertical structures. On the

contrary, Wenner-Schlumberger array is more sensitive to vertical changes and good at mapping horizontal structures (Loke, 2013).

One measurement may contain hundreds or thousands of injection times, by numbering all the electrodes, the input sequence examples for the measurement is shown in Figure 5.3.

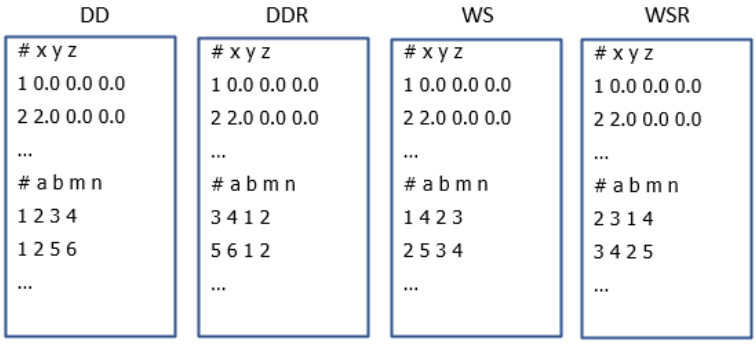

Figure 5.3: Examples of input sequence for different array types

5.3. ERT inversion theory

The theory for electrical resistivity inversion is based on the work done Günther *et al.* (2006). The measured data from ERT is the apparent resistivity, and the target results are the estimated field resistivity model. The aim of performing ERT inversion is to find a resistivity model that fit best to the true resistivity distributions. During the process of parameter estimation, least squares fitting is commonly used (Chavez Olalla *et al.*, 2021), to minimize the squared error between the simulated and measured resistivity values (Wiekenkamp, 2012).

6

Methodology

6.1. Field experiment

The field experiments were conducted in March, May and August. The main task was to perform a series of electrical resistivity surveys on the landfill subsurface. Measurements of water levels and multiple GPS coordinates were also required to provide additional data for the ERT results.

6.1.1. Electrical resistivity surveys

The electrical resistivity surveys were carried out with the IRIS Syscal Pro machine. The electrodes were installed in five lines in the landfill cell 3. The layout and the field photos are presented in Figure 6.1. The figure on the upper left gives an overview of five electrical resistivity measuring lines; the figure on the bottom left is the field photo of ERT Line 3−5; the figure in the middle is the locations of ERT electrodes from the measured GPS data plotted in the software QGIS (in which red dots, purple dots, cyan dots, yellow dots, green dots are Line 1−5 respectively; orange dots are the twelve ERT wells; and blue dots are piezometer wells); and the figure on the right is the field photo of ERT

Line 1 (including electrodes, orange cables and Syscal machine).

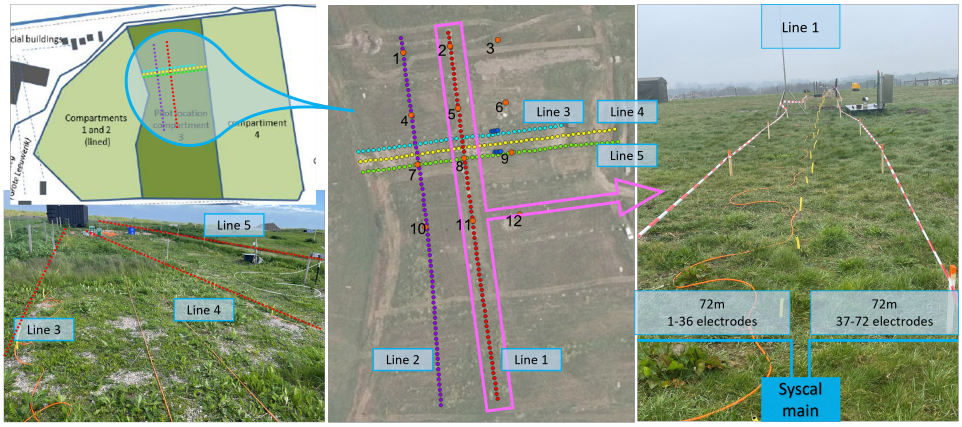

Figure 6.1: The layout of ERT lines in the landfill Kragge cell 3.

The places of measurement lines were chosen based on where water level in the wells had obvious diversification. Meanwhile, to compare the obtained resistivity values with the wells water level data, lines were designed to pass through several wells. Therefore, the spacing between the two 'vertical' lines: Line 1 and Line 2 is approximately $18m$, which is the distance between two ERT wells in the east-west direction. To explore the changes in a smaller scale, the three 'horizontal' lines are all $4m$ apart.

The lengths of every line was determined by multiple factors. Firstly, the maximum depth that ERT method can detect is reached at the midpoint of the line, which is about 20% of the line length for dipole-dipole array (Furman *et al.*, 2003). Given that the average elevations of the landfill bottom liner and top surface are roughly $6.5m$ and $27.5m$ respectively, the length of the lines should be at least $105m$. Secondly, it is wise to make full use of the measurement cables to which machine can be connected. For Syscal Pro main machine, there are 72 electrode connection points. Meanwhile, to make sure that the results on each line had sufficient resolution, based on experience, the electrodes were inserted into the landfill cover layer every $2m$. The two lines from north to south (marked as Line 1 and Line 2) were $142m$ long. Moreover, perpendicular to these lines, the field size brought about some restrictions that

the landfill cell 3 has a maximum width of 100m, and there is a fixed container blocking at the end of Line 3. Taking account of all these factors, the length of Line 3 was chosen to be 78m, and that of Line 4 and Line 5 was 98m, correspondingly, the number of electrodes was 40, 50 and 50 for each line.

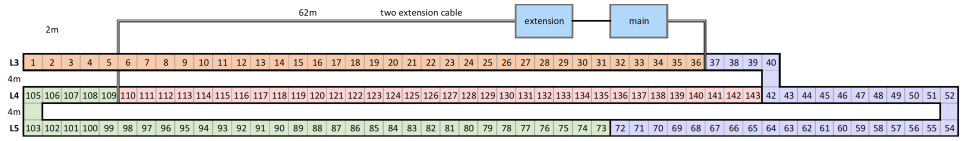

Figure 6.2: The connection mode of ERT Line 3, Line 4 and Line 5.

Table 6.1: Experimental layout of ERT lines.

Lines name	Length (m)	Electrodes No.	Electrodes interval (m)	Wells included
Line 1	142m	72	2m	ERT_wells 2 5 8 11
Line 2	142m	72	2m	ERT_wells 1 4 7 10
Line 3	78m	40	2m	P1.3-P1.13
Line 4	98m	50	2m	–
Line 5	98m	50	2m	ERT_wells 7 8 9 P2.3-P2.13
Notes:	The distance between Line 1 and Line 2 is around 18m The distance between Line 3, Line 4 and Line 5 is around 4m			

With regard to the connection strategy, Line 1 and Line 2 were measured separately by connecting the 72 electrodes directly to the Syscal main machine with two cables. The connection procedure of the three 'horizontal' lines was more complicated. With the assistance of Syscal extension machine, the cable connection points is expanded to reach a maximum number of 216, so that three lines can be measured at the same time. The 140 electrodes required four cables with 36 connection points each, which are marked with four different colors in Figure 6.2. In this schematic diagram, the serial number in each grid represents the order of electrode connection. One connection point

was skipped every time the cable was switched between two lines, for the reason that the distance between two 'horizontal' lines is $4m$ while the distance between two cable connection points is only $3m$. Finally, the experimental arrangements of ERT lines are listed in Table 6.1.

Table 6.2: Parameters of IRIS Syscal Pro machine setup.

Max. elect.		72 (main) & 144 (extension)
Cable connection points		18 or 36
Configuration	mode	Automatic sequence
	Stack/Q	Stacks min=5, max=10 Qmax=2
	Options	Reading: average Voltage: signed IP values: default Spacing unit: meter
	T_x parameters	Rho (Resistivity only) Time: $500msec$ $V\|I_{ab}$ = $200V$
	E.array	e.g. dipole-dipole Nb channel: 10

The settings of the Syscal Pro device was established pursuant to the desired results and the previous experience(Table 6.2). The number of repeated measurements was determined by the 'Stack/Q' option. The quality factor (Q) is the standard deviation of the V_{mn}/I_{ab} ratio measured during the repeated measurements under the same array. If the measured value is larger than the introduced value, then the number of stacks (cycles) will run up to the defined maximum number of stacks , otherwise only the minimum number of stacks is needed. The current was injected with a constant voltage value ($V|I_{ab}$ requested = $200V$), and the time for the injection is $500msec$. Those main control parameters guaranteed the electrical resistivity survey had more

stable and valid results.

According to the fact that the distribution of leachate in the landfill is highly heterogeneous and non-continuous (refer to Chapter 2), both horizontal and vertical changes in the water body should be taken into account, therefore both dipole-dipole array and Wenner-Schlumberger array were applied. To quantify the electrical resistivity measurement errors, several reciprocal arrays were tested as well. A list of all the measurements that have been conducted is given in Table 6.3. Line 1 and Line 2 were measured individually using dipole-dipole array, Wenner-Schlumberger array and their reciprocal arrays. Line 3, Line 4 and Line 5 were measured jointly with a single input sequence file that combined these four arrays.

6.1.2. Wells water level measurement

The water level of ERT wells and piezometer wells were measured by manually dipping the wells, to provide some reference of the ERT results. The instrument is called dip meter or water level indicator. It has a sensor probe at the lower end of the tape, which has an electrically insulated gap that will be connected once it comes in contact with water. When this contact occurs, the buzzer in the dip meter will go out and the indicator light will light up.

In order to detect the water surface, the probe was immersed in the well and lowered to the position where the buzzer and light indicated the presence of water. This step was repeated a few times in a slow manner to get the water depth from the tape as accurate as possible. The depth of the well was measured by lowering the same probe completely to the bottom of the well until the tape was no longer taut. The calculation of the water level to NAP is identical to Equation 2.1.

6.1.3. GPS measurement

The GPS survey was required for several reasons. First of all, having precise coordinates of ERT pins is essential to track back the experiment locations as well as to depict the tomography of ERT lines. Besides, electrical resistivity inversion process also requires the specifics of the set points.

Table 6.3: Lists of electrical resistivity measurements results in the Landfill Kragge.

Date	Line name	Array type	Measurement time (h)
2021 March 24	Line 1	dipole-dipole	1.5h-2h
	Line 1	dipole-dipole reciprocal	1.5h-2h
	Line 1	Wenner-Schlumberger	1.5h-2h
2021 March 25	Line 2	dipole-dipole	1.5h-2h
	Line 2	Wenner-Schlumberger	1.5h-2h
2021 May 17	Line 1	dipole-dipole	1.5h-2h
	Line 1	Wenner-Schlumberger	1.5h-2h
	Line 1	Wenner-Schlumberger reciprocal	1.5h-2h
2021 May 18	Line 2	dipole-dipole	1.5h-2h
	Line 2	Wenner-Schlumberger	1.5h-2h
	Line 2	Wenner-Schlumberger reciprocal	1.5h-2h
2021 May 21	Line 3 Line 4 Line 5	Combined four arrays	6h-7h
2021 August 12	Line 2	dipole-dipole	1.5h-2h
	Line 2	Wenner-Schlumberger	1.5h-2h
2021 August 13	Line 1	dipole-dipole	1.5h-2h
	Line 1	Wenner-Schlumberger	1.5h-2h

Additionally, the GPS of various wells and infiltration systems are needed to be defined on the ERT results.

TRIMBLE R8-2 PPK/RTK was used to detected the GPS. The main components consist of Trimble R8 receiver, TSC2 data collector, and a 2-meter-long carbon connecting pole with level. With Real Time Kinematic (RTK) method, real-time base data was linked with a nearest service provider by satellites.Raw measurements were processed by the receiver and stored in the TSC2 data collector. The resulting data were 3D coordinates, where X and Y coordinates were expressed as North and East in the coordinate reference system (CRS): EPSG:28992 Amersfoort / RD New, Z coordinate was the point elevation to NAP.

6.2. ERT Data quality assessment

6.2.1. General estimation

The relevant elements to be considered contain the errors, geometric factors, resistance and apparent resistivities. Those values should be evaluated in order to remove the useless or invalid data.

Initially, the accurate electrode positions were not included in the exported result files, therefore they should be corrected from the GPS measurement. After that, the geometric factors for every acquisitions were calculated from Equation 5.9, the resistance and the apparent resistivities were obtained according to Equation 5.10 and Equation 5.10, where I and $\Delta\phi$ are the current (I) and the voltage (U) collected by the ERT system correspondingly. The errors in the results are used for weighting (Günther *et al.*, 2006), which appears in the denominator in the data functional (refer to equation ?), so the errors equalled to zero was adapted to the minimum error other than zero.

The general calibration was intended to exclude the extreme values. For the resistance measured in each time, a confidence interval of 95.4% was recommended, which means that only the values within twice the standard deviation around the average values were retained. Besides, the results were regarded as valid only when: (a) the systematic measured error was under 20.0, (b) the absolute values of geometric factor was below 10000 and (c) the

apparent resistivity was no less that $0.15\Omega \cdot m$.

6.2.2. Reciprocal error evaluation

The main applied array is considered as the normal array, and the corresponding control group is its reciprocal array. During the reciprocal measurement, only the current and potential (voltage) electrode pairs were interchanged, then the measured results from the selected array and its reciprocal array should be identical under ideal conditions. However, since the current injection and voltage measurement were at different electrode pair, the calculated resistance in reality is rather a transfer resistance, which is a average result along the current injection to the potential measurement path. This path differ even under the same array sequence, so that the magnitudes of the resistance also generate some variations under normal and reciprocal array. Moreover, each measurement took a relatively long time (about 2 hours per measurement), during this period, some infiltration lines were tested, the rainfall and evaporation was frequent, so the water in the landfill waste body appeared to have some small amount of fluctuations.

Analyzing the reciprocal errors helps quantify the uncertainty of observations and evaluate the data quality (Zhou and Dahlin, 2003). For each measurement, the average resistance ($\overline{R}$) was counted by Equation 6.1:

$$\overline{R} = 0.5\,(R_n + R_r) \tag{6.1}$$

Where R_n is the resistance from the normal array and R_r is the resistance from the correlated reciprocal array.

The reciprocal error (ϵ_{nr}) was defines as the discrepancy between the normal and reciprocal resistance, which is:

$$\epsilon_{nr} = R_n - R_r \tag{6.2}$$

Then the data was removed from the ERT dataset when the reciprocal errors were larger than 10% of the average resistance (Korteland, 2013, Korteland and Heimovaara, 2015). The calculation was operated based on the absolute values, namely:

$$|\epsilon_{nr}| \geq 0.1|\overline{R}| \tag{6.3}$$

The ERT datasets for the inversion were thought to be robust after filtering those misfit resistance. The measurements with the reciprocal control groups were: Line 1 dipole-dipole array on 2021 March 24, Line 1 Wenner-Schlumberger array on 2021 May 17 and Line 2 Wenner-Schlumberger array on 2021 May 18. For other measurements without the reciprocal survey, only the criterion described in the Section 6.2.1 were examined.

6.3. Electrical resistivity inversion

The inversion theory was based on Günther *et al.* (2006), Rücker (2010). The python package 'pyBERT' (Günther and Rücker, 2013) and 'pyGIMLi' (Rücker *et al.*, 2017) were used to solve the inversion problem. Boundless Electrical Resistivity Tomography (BERT) aims to work on arbitrary geometries, the unstructured finite element meshes are used for forward calculation and parameter identification, so there is no order or rule of shape for the elements (Günther and Rücker, 2013, Rücker *et al.*, 2006). pyGIMLi is an open-source library for modelling and inversion and in geophysics. One main task of pyGIMli is to perform inversion based on the generalized Gauss-Newton method (Rücker *et al.*, 2017). Triangle mesh was used for inversion, so that the tomography of along the measurement lines were depicted from GPS coordinates, the inversion parameters are listed in Table 6.4.

Table 6.4: Parameters of ERT inversion.

Parameter	Value	unit	Physical meaning
lam	20	–	Regularization strength
paraDX	0.2	m	Size (in electrode spacings) of cells at the surface
paraMaxCellSize	1	m^2	Maximum cell size area (DIMENSION=2) for para mesh
paraDepth	30	m	Maximum depth of parameter domain
quality	33.6	–	How fast the mesh is growing (33-fast,35-slow)

Initially, the electrical resistivity inversion was performed with single array

('standard inversion'). Then, the measurement results using different arrays for the same line and the same date were superimposed in one file and inversed, which is called 'joint inversion' in this thesis.

6.4. Results analysis

6.4.1. Preparation work

In order to read the resistivity data from coordinated with flexibility, the triangle meshes were converted into square grids, with a size of $0.1m \times 0.1m$. The python package 'Scipy' were used during this step (Virtanen *et al.*, 2020). With the 'cubic(2-D)' option, it return the value determined from a piecewise cubic, continuously differentiable, and polynomial surface with minimal approximate curvature (Virtanen *et al.*, 2020).

Then the positions of ERT wells, piezometer wells, water level in the wells, bottom liner and cross-section of infiltration lines are explored on the inversion results.

6.4.2. Laplacian edge detection

Laplacian edge detection is an edge detection technology, which aims at identifying the points in an image where the values indicate the sharpest changes. These points can be searched numerically where the second derivatives of the 2D image equal to zero . Then the edges are formed by those recognized points. The basic Equation is:

$$\nabla^2 Z\,(x,y) = \frac{\partial^2 Z}{\partial^2 x} + \frac{\partial^2 Z}{\partial^2 y} = 0 \tag{6.4}$$

where $Z\,(x,y)$ represents for the resistivity values, x and y gives the horizontal and vertical coordinates of the target points.

In practical application, the python package 'Scipy' was used (Virtanen *et al.*, 2020), which uses N-D Laplace filter based on approximate second

derivatives, the discretized Laplacian operator is expressed as:

$$LAP = \begin{bmatrix} 0 & 1 & 0 \\ 1 & -4 & 1 \\ 0 & 1 & 0 \end{bmatrix} \tag{6.5}$$

Besides, the processes of ERT inversion and mesh interpolation may generated fake edges and artifacts, while the Laplacian operator is quite sensitive to small noise, so the grid results should be further smoothed by the Gaussian filter (Chavez Olalla *et al.*, 2021). Gaussian blur (also called smoothing blur) is an image processing method to blurring the image by the Gaussian function. An appropriate filter strength was picked based on the Laplacian edge detection results (Chavez Olalla *et al.*, 2021). This step was also realized by the python package 'Scipy' (Virtanen *et al.*, 2020).

6.4.3. Water retention curve

This step aims to find a suitable correlation to describe the resistivity and water head values. The water in the waste body was assumed to be hydrostatic. And the interface of the dry and wet bulks were considered to be where the resistivity was equal to $20\Omega \cdot m$. Firstly, the resistivity values from a mass of random points were read from the ERT inversion maps with converted grids. The water pressure heads were the distance between the selected points and the contour that the resistivity was $20\Omega \cdot m$ in the vertical direction. These two variables are taken as the measured results. Then, the theoretical relations between the resistivity and water pressure head were modeled based on Archie's law (Archie, 1942) and van Genuchten equation (Van Genuchten, 1980).

To begin with, Archie's law is written in Equation 6.6, it gives an empirical relation between resistivity values and water saturation.

$$\rho_a = A\rho_w \phi^{-M} S_w^{-N} \tag{6.6}$$

in this equation, ρ_a is the waster body target resistivity and $\rho_w$is the leachate resistivity. ϕ is the porosity of the waste and S_w is the degree of saturation. A, M and N are empirical parameters, which should be estimated. The degree of

saturation (S_w) is defined by Equation 6.7:

$$S_w = \frac{\theta_w}{\phi} \tag{6.7}$$

where θ_w is the water content. It can be derived from the definition of the effective saturation (S_{eff}):

$$S_{eff} = \frac{\theta_w - \theta_{res}}{\theta_{sat} - \theta_{res}} \tag{6.8}$$

where θ_{res} and θ_{sat} are the residual water content and saturated water content respectively.

On the other hand, the effective saturation (S_{eff}) can be calculated from the van Genuchten equation, which couples the water content to capillary pressure head:

$$S_{eff}(h_c) = \begin{cases} [1 + (\alpha h_c)^n]^{-m} & h_c > 0 \\ 1 & h_c \leq 0 \end{cases} \tag{6.9}$$

α, n and m are empirical parameters to be estimated, where α is the reciprocal of capillary head at half saturation, n determines the sloop of the water retention curve, and m is calculated from n:

$$m = 1 - \frac{1}{n} \tag{6.10}$$

h_c is the capillary pressure head obtained from Equation 6.11:

$$h_c = h_a - h_w \tag{6.11}$$

where h_a is the air pressure head which is assumed to be equal to zero everywhere ($h_a == 0.0m$), h_w is the water pressure head. It is assumed that a certain resistivity contour gives the boundary between wet and dry areas, then the water pressure head is the vertical distance away from the interface contour under hydrostatic situations. At the interface, the pressure head is zero, and the unsaturated place result in the negative pressure head. A schematic diagram to calculate the water pressure head is shown in Figure 6.3. In practice, the calculating points were picked every $1m$ in the horizontal direction and every $0.1m$ in the vertical direction from the resistivity inversion maps.

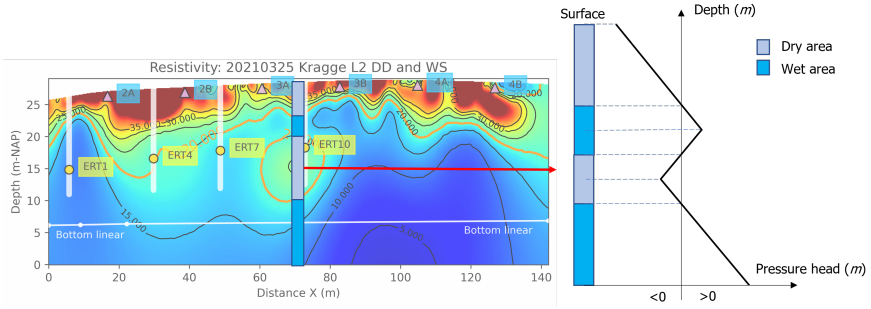

Figure 6.3: A schematic diagram of water pressure head in a column.

The final aim is to express the resistivity by the water pressure head, which is given by:

$$\rho_a = a\rho_w\phi^{-M}\left[S_{eff}\left(-h_w\right)\left(1-S_{res}\right)+S_{res}\right]^{-N} \tag{6.12}$$

There are in total eight unknown parameters in this equation. The values of parameters were tested manually, the calculated curves were supposed to fit the measured resistivity-water pressure head curves.

7

Results

7.1. Data quality assessment

Taking the measurements of Line 1 using the dipole-dipole array and its reciprocal array on 2021 March 24 as an example, the primary data of the resistance, apparent resistivities, measurement errors and geometric factors are plotted in Figure 7.1. The majority of the initial results from the normal array were much the same as its reciprocal array, and most of the measurement errors were small, which proved the overall validity of the measurements. However, there remained some sequence appearing remarkable measurement errors and reciprocal errors.

After removing the resistance values that were not within the 95.4% confidence interval, the number of measurements reduced from 2875 to 1860 in the dipole-dipole array dataset. Then this number reduced further to 1599 when the noise with large reciprocal errors were eliminated. Besides, if only the reciprocal errors were removed without considering the confidence interval of resistance, the number of measurement in ERT dataset still reduced to 1668. This indicates that most of the places with large model uncertainty were also the places with large reciprocal errors.

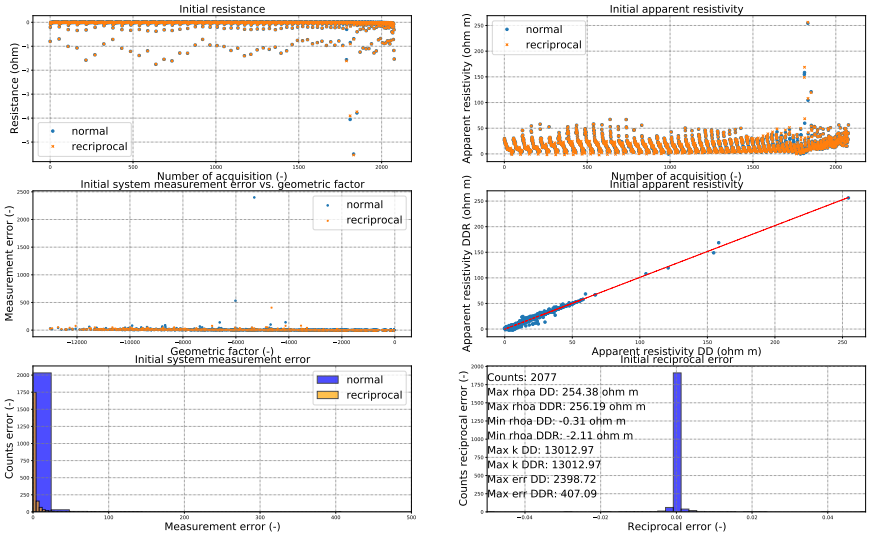

Figure 7.1: Comparison of initial ERT data for Line 1 dipole-dipole array between its reciprocal array on 2021 March 24.

The processed data are shown in Figure 7.2. The top two subfigures suggest that the resistance and apparent resistivity values from the normal array became closer to those from the reciprocal array after the reciprocal errors being sorted, and the ranges of apparent resistivities for the two arrays were restricted from $3.15\Omega \cdot m$ to $58\Omega \cdot m$ and from $3.10\Omega \cdot m$ to $57.92\Omega \cdot m$ sequentially. The differences of apparent resistivities counting from every acquisition floated narrowly in $\pm 3\Omega \cdot m$ and follow normal distribution after being processed. The remaining system measurement errors were limited to less than 20 and also obeys Gaussian distribution. In addition, the system measurement errors had a tendency to increase with the increase in geometric factors. Since the geometric factors only depend on the coordinates of the four electrode pairs used at each sequence, this trend reflects that the increase in the depth led to broader measurement uncertainty.

From another perspective, the pseudo sections of apparent resistivities are able to illustrate the influence of the data filtering on apparent resistivities more locally and intuitively (Figure 7.3). The continuity of image pixels indicates that the measurement had a high spatial resolution, which is good. Although

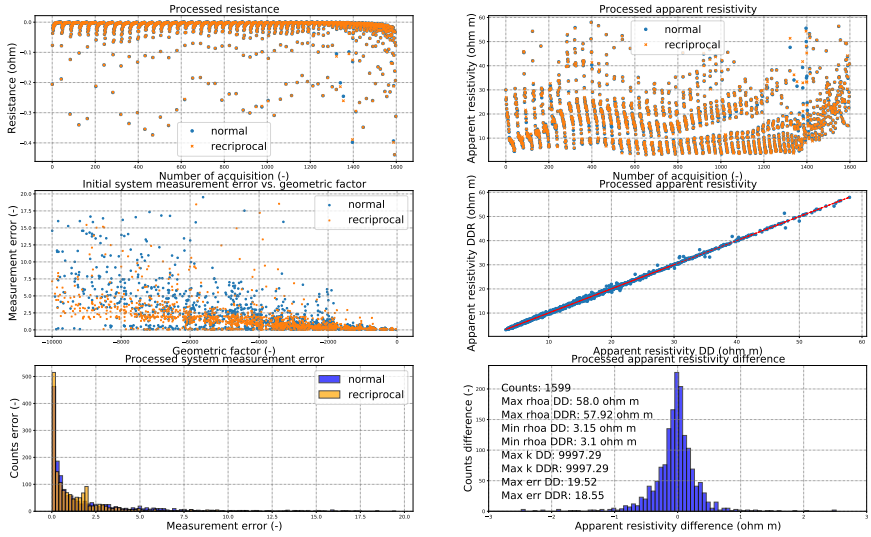

Figure 7.2: Comparison of processed ERT data for Line 1 dipole-dipole array between its reciprocal array on 2021 March 24.

the vertical axis of the plots represents the array level rather than the depth, the horizontal axis expresses the true distance at the surface. The pseudo sections indicate that there was an abnormal area around $90m$ to $96m$ from the starting point in the horizontal direction, which led to the appearance of exaggerated measurement errors and reciprocal errors over depth in this area. Excluding the resistance values that deviated from the average by more than twice the standard deviation only got rid of the apparent resistivity outliers in single datasets. Only after filtering the reciprocal errors, the remained apparent resistivity data were identical between the normal array and its reciprocal array, and this procedure seems to indicate that most of the misfit originated from this anomalous area in the surface.

The other two dot results with the reciprocal surveys were the measurement on Line 1 using Wenner-Schlumberger array on 2021 May 17 and the measurement on Line 2 using Wenner-Schlumberger array on 2021 May 18. The scatter plots and histograms of their processed data (including resistance, apparent resistivities, errors and geometric factors) are shown in Figure 7.4 and Figure 7.5. Those plots also demonstrate that in general,

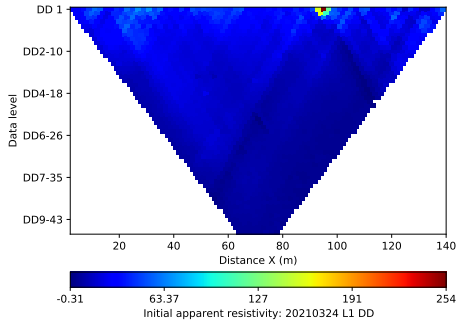

(a) Pseudo section of normal array from raw data

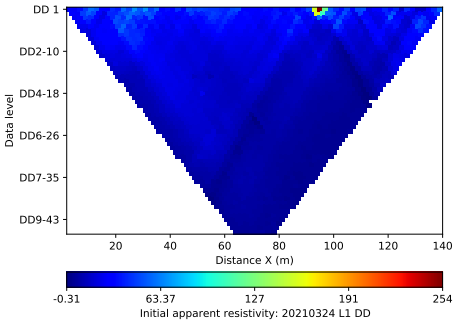

(b) Pseudo section of reciprocal array from raw data

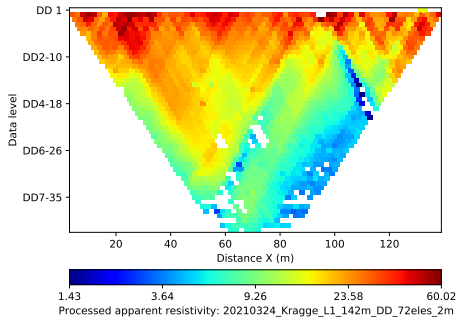

(c) Pseudo section of normal array for resistance within confidence interval

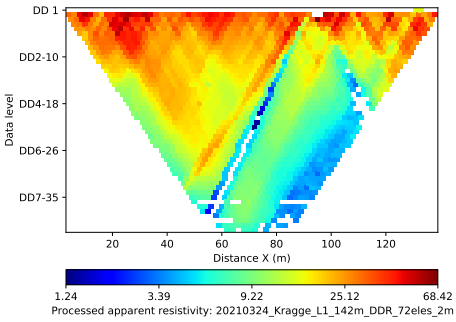

(d) Pseudo section of reciprocal array for resistance within confidence interval

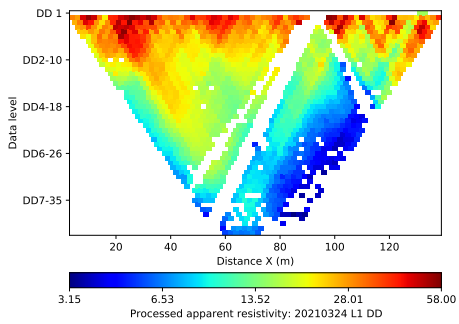

(e) Pseudo section of normal array after removing large reciprocal errors

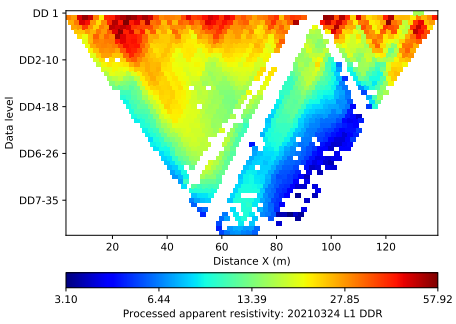

(f) Pseudo section of reciprocal array after removing large reciprocal errors

Figure 7.3: Pseudo sections of Line 1 dipole-dipole array and its reciprocal array on 2021 March 24.

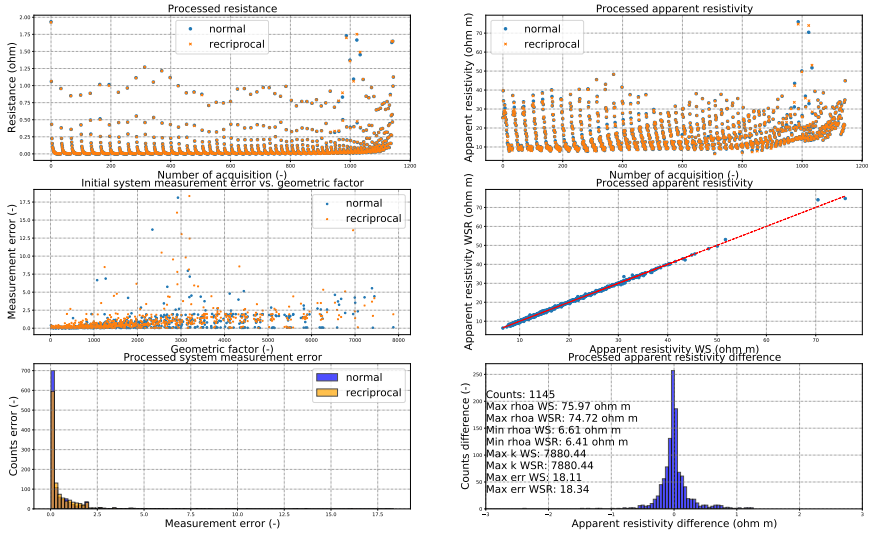

Figure 7.4: Comparison of processed ERT data for Line 1 Wenner-Schlumberger array between its reciprocal array on 2021 May 17.

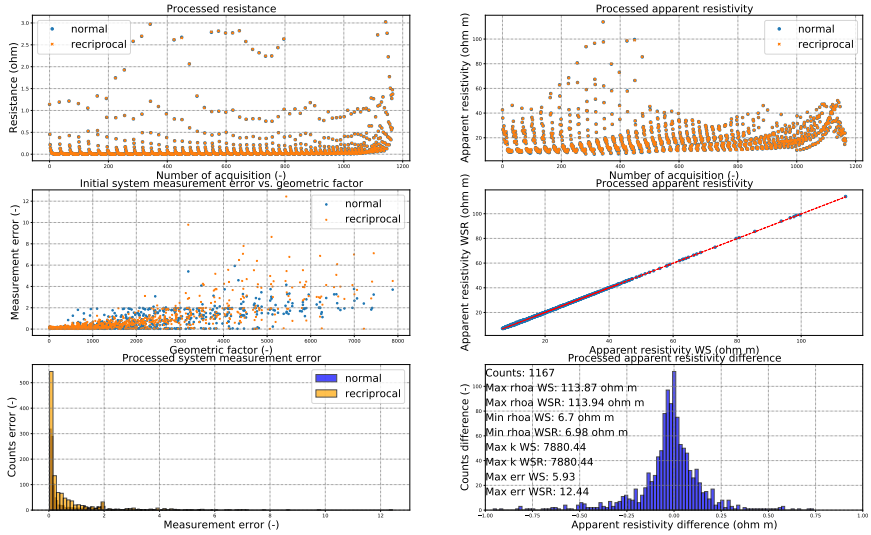

Figure 7.5: Comparison of processed ERT data for Line 2 Wenner-Schlumberger array between its reciprocal array on 2021 May 18.

the measurement errors and the reciprocal errors are normally distributed. Similarly, the apparent resistivities of the other two sets of measurements can be displayed in the form of pseudo section, which are shown in Figure 7.6. The pseudo sections delineate the similar extremely high resistivity areas in Line 1, while only 100 measurement points were removed and eliminated, and most of these points were concentrated on the surface, which can also be illustrated in line with the sensitivity depth of Wenner-Schlumberger array, that this array is less contaminated by noise than the other electrode arrays (Dahlin and Zhou, 2004). In other words, the Wenner-Schlumberger array higher signal-to noise ratio than other configurations (Falae *et al.*, 2019).

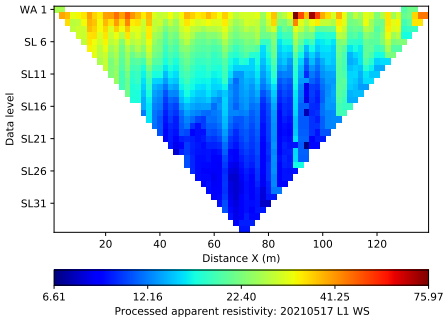

(a) Pseudo section of Line 1 normal array on 2021 May 17

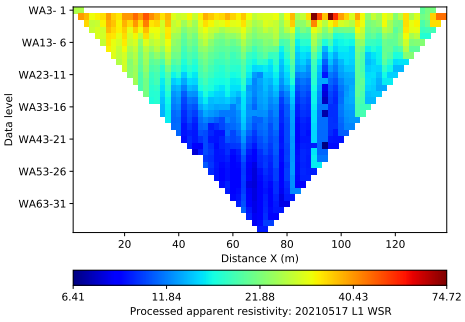

(b) Pseudo section of Line 1 reciprocal array on 2021 May 17

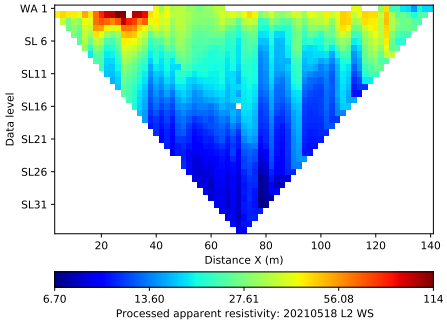

(c) Pseudo section of Line 2 normal array on 2021 May 18

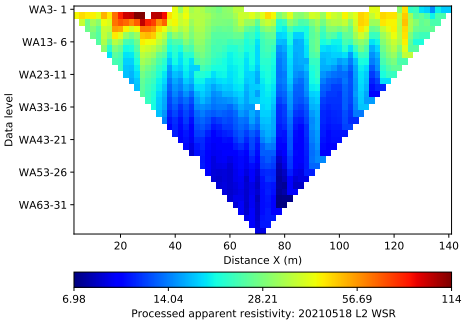

(d) Pseudo section of Line 2 reciprocal array on 2021 May 18

Figure 7.6: Pseudo sections of Wenner-Schlumberger array after sorting the reciprocal errors.

Overall, the data uncertainty mainly rooted in the abnormal area on the surface. This uncertainty may be due to a long period of Infiltration and rainfall compared to the long measurement time, so that the condition of the landfill water content was changing during the survey. Besides, the anomaly may also arose from the contact problem of electrodes, that the pins may disconnect with soil at a very dry part in the surface. This possibility urged us to go back to inspect the field again, and it is suggested that the salt solution could be added surrounding the dry surfaces for the further measurement. Outside of the anomaly region, most of the measurement points were retained, which means that generally the data were of sufficient quality.

7.2. ERT Inversion results

7.2.1. Initial mesh results

The ERT data were firstly inversed using the separate dataset and then using the dataset that combined results both the dipole-dipole array and the Wenner-Schlumberger array. The inversion results of Line 1 and Line 2 in March are shown in Figure 7.7 and Figure 7.8.

The results of the normal and reciprocal measurements after filtering the reciprocal errors looked almost the same. Some differences appeared when the depth increased, which came from the larger errors input at the bottom (Figure 7.7(a) and Figure 7.7(b)). The results also illustrate the characteristics of the different arrays, that the dipole-dipole array is good at detecting the vertical structures (Figure 7.7(a) and Figure 7.8(a)), while the Wenner-Schlumberger array tends to be good at detecting the vertical changes and is relatively insensitive to the horizontal changes. Under the same horizontal distance, the depth that could be detected using Wenner-Schlumberger array is more shallow (Figure 7.7(c) and Figure 7.8(b)). The superimposed datasets could take advantages from both arrays (Figure 7.7(d)).

Electrical resistivity inversion results show that the distribution of the waste body leachate maintained a consistent pattern over time. The landfill dried out slightly after entering the summer, so the apparent resistivities were slightly

reduced overall. On the whole, in the vertical direction, the inversed apparent resistivities were higher at the surface and lower at the bottom, indicating that the water accumulated at the bottom. The resistivities exhibited considerable fluctuations in the horizontal direction, which seemed to indicate that the water level was continuously fluctuating. When looking into the ERT inversion maps of Line 2, it is obvious that the resistivities formed a high-resistance elliptical block, with center coordinates approximately at $(70m, 15m)$, which was surrounded by the low resistivity area below the top high-resistance layer. The measurements of the three 'horizontal' lines were only carried out in May. Moist plumes appeared similarly on these three lines at horizontal distances of approximately $0m$, $40m$ and $80m$, nevertheless, the resistivity distribution pattern varied out even though the distances between those 'horizontal' lines were merely $2m$.

In a word, the initial inversion results verified that the application of ERT realized the qualitative visualization, to delineate the depth and lateral extension of the local dry and wet plume (Clément *et al.*, 2011). The information of field physical properties that could be read from the ERT maps was limited. Since the results from joint arrays were able to absorb the advantages of both arrays, the following analysis would mainly be based on the joint arrays.

7.2.2. ERT converted grid results

Figure 7.10 gave the comparisons between the mesh results and grid results of Line 1 and Line 2 measured in March. The results show that the converted grid results were almost identical to the initial ERT maps which used mesh to inverse, in both large-scale changes and even small details. Since the grid size was $0.1m$ by $0.1m$ square, which was greatly smaller than the triangular mesh size that was used during the inversion, which was $1m^2$, the processed map show more smoothness. The color scale of the figures were limited ranging from $0\Omega \cdot m$ to $50\Omega \cdot m$ isometrically. Then the graphs more clearly depict that the landfill waste body transferred from dry to wet condition when the apparent resistivities were around $20\Omega \cdot m$.

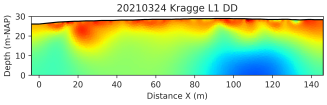

(a) ERT inversion results of Line 1 using the dipole-dipole array

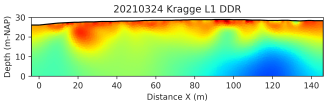

(b) ERT inversion results of Line 1 using the dipole-dipole reciprocal array

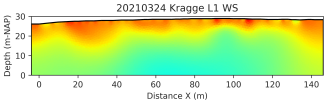

(c) ERT inversion results of Line 1 using the Wenner-Schlumberger array

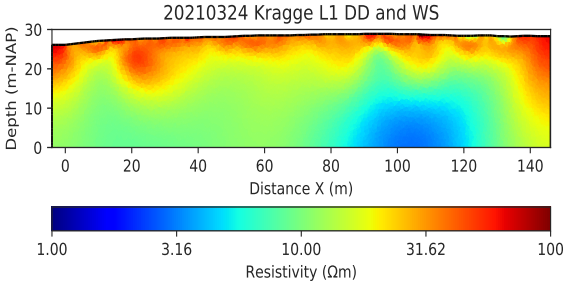

(d) ERT inversion results of Line 1 using joint arrays

Figure 7.7: ERT inversion maps of Line 1 on 2021 March 24

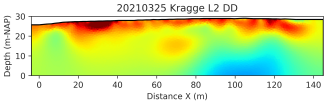

(a) ERT inversion results of Line 2 using the dipole-dipole array

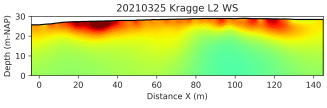

(b) ERT inversion results of Line 2 using the Wenner-Schlumberger array

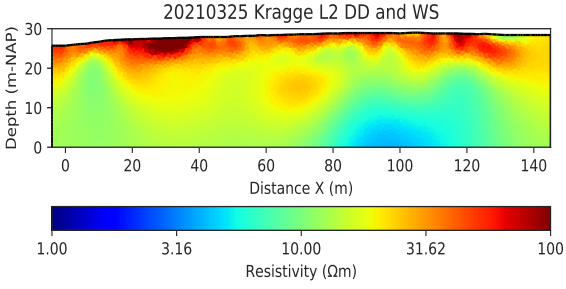

(c) ERT inversion results of Line 2 using joint arrays

Figure 7.8: ERT inversion maps of Line 2 on 2021 March 25

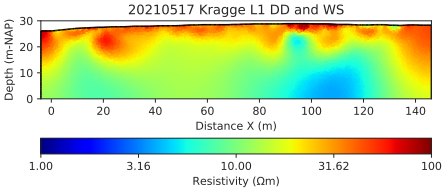

(a) ERT inversion results of Line 1 using joint arrays on 2021 May 17

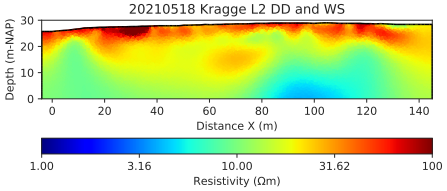

(b) ERT inversion results of Line 2 using joint arrays on 2021 May 18

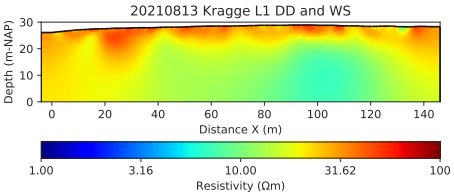

(c) ERT inversion results of Line 1 using joint arrays on 2021 August 13

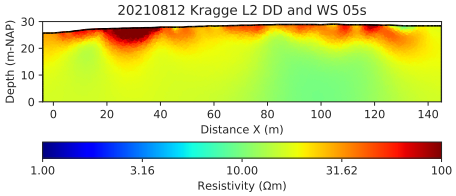

(d) ERT inversion results of Line 2 using joint arrays on 2021 August 12

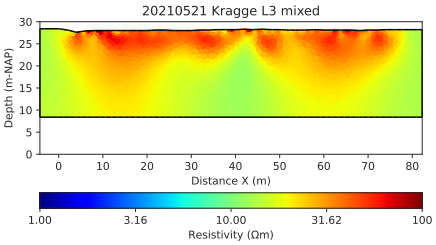

(e) ERT inversion results of Line 3 using joint arrays on 2021 May 21

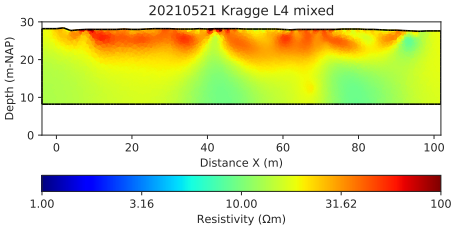

(f) ERT inversion results of Line 4 using joint arrays on 2021 May 21

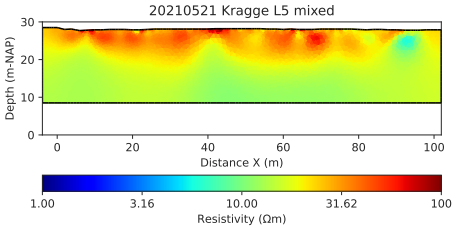

(g) ERT inversion results of Line 5 using joint arrays on 2021 May 21

Figure 7.9: ERT inversion maps for the rest of all measurements with joint arrays.

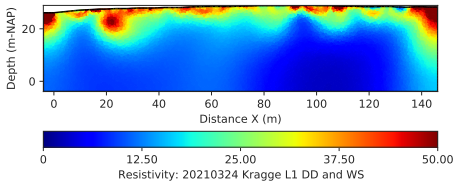

(a) Mesh ERT inversion results of Line 1 using joint arrays on 2021 March 24

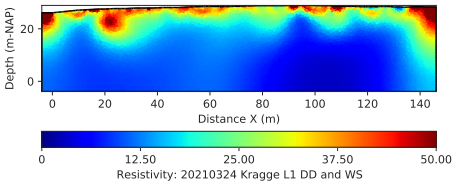

(b) Grid ERT inversion results of Line 1 using joint arrays on 2021 March 24

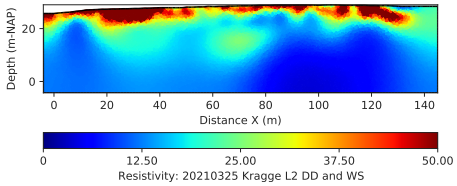

(c) Mesh ERT inversion results of Line 2 using joint arrays on 2021 March 25

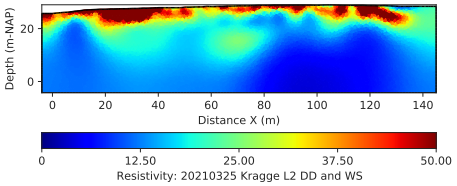

(d) Grid ERT inversion results of Line 2 using joint arrays on 2021 March 25

Figure 7.10: Comparison of ERT inversion mesh maps and their converted grid maps of Line 1 and Line 2 measured in March.

7.3. Laplacian Edge detection

Figure 7.11 presents the ERT maps after applying the Laplacian edge detection. In each plot, the infiltration channels were marked with triangles and their corresponding names, for example, '2A' and '2B'. The position and the depth of ERT wells and piezometer wells were represented by the white vertical column, and the yellow dots noted in the column described the places where the dip meter detected the existence of water. The contour lines with the same apparent resistivity value were in black, and the contour line where the apparent resistivities were $20\Omega \cdot m$ were bolded. The subfigures in the left column showed the contour lines that were detected according to the Laplacian operator (in multiple colors), and the subfigures in the right column showed the contour lines where the first derivative (in fuchsia) and the second derivative (in orange) of apparent resistivities were manually calculated to be zero in each vertical columns.

From the results, the Laplacian edge detection method failed to discover

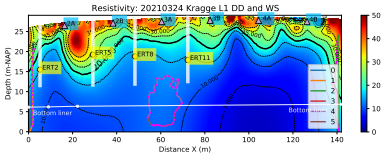

(a) Laplacian edge detection applied to Line 1 using joint arrays on 2021 March 24

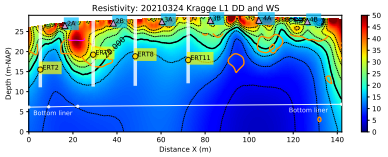

(b) Manual derivative calculation applied to Line 1 using joint arrays on 2021 March 24

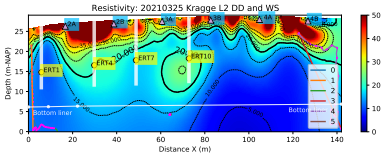

(c) Laplacian edge detection applied to Line 2 using joint arrays on 2021 March 25

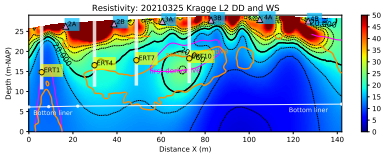

(d) Manual derivative calculation applied to Line 2 using joint arrays on 2021 March 25

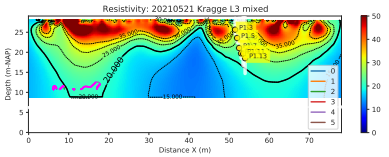

(e) Laplacian edge detection applied to Line 3 using joint arrays on 2021 May 21

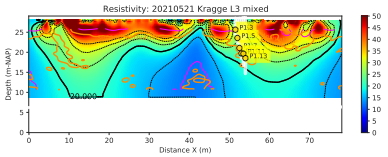

(f) Manual derivative calculation applied to Line 3 using joint arrays on 2021 May 21

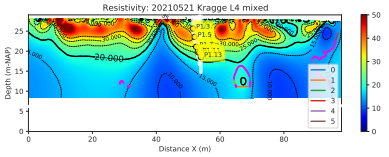

(g) Laplacian edge detection applied to Line 4 using joint arrays on 2021 May 21

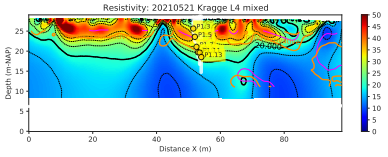

(h) Manual derivative calculation applied to Line 4 using joint arrays on 2021 May 21

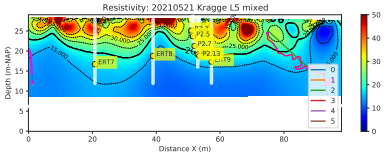

(i) Laplacian edge detection applied to Line 5 using joint arrays on 2021 May 21

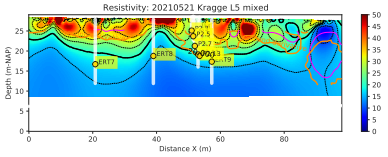

(j) Manual derivative calculation applied to Line 5 using joint arrays on 2021 May 21

Figure 7.11: Applying Laplacian edge detection technology and manual derivative calculation to the ERT inversion results after converting the grids.

the interface of water transaction zones nor the leachate flow trends, due to the fact that the water distribution in the waste body was highly heterogeneous, while the Laplacian operator tends to distinguish the different layers with significant property changes. Considering the hypothesis of preferential flow, the water level in the wells didn't represent the interface of water surface, since there widely distributed plenty of barriers in the landfill.

7.4. Resistivity and water head analysis

From the resistivity inversion maps, the contour lines with resistivities equal to $20\Omega \cdot m$ could distinguish the ideal interface of dry parts and wet parts in the waste body. Therefore, the places where resistivity values were less than $20\Omega \cdot m$ were considered to be unsaturated, corresponding to the negative water pressure head. The set of parameters to compute the resistivities from Archie's law and van Genuchten equation are listed in Table 7.1. Two groups of fitting data were selected, each containing four scenarios. In Figure 7.12, the resistivity and water pressure head values read from the ERT maps were plotted in multi-colored dots, and the theoretical fitted curves were plotted in black color.

The figures show that in the saturated situations, the increase of positive water pressure heads resulted in similar resistivity values, because the same saturated water content corresponds to a single resistivity value. Under unsaturated conditions, the continued decrease of the negative water pressure heads increased the resistivity. However, the figure also shows that in the unsaturated parts, the apparent resistivities did not always increase exactly as the pressure head became more negative in some situations. Figure 7.14(a) gives the relationships between water pressure head and resistivity with the depth reading from the resistivity inversion maps only when the horizontal distance is between $128m$ and $140m$ (every $5m$) on Line 2. From top to bottom, it can be seen that the water pressure heads changed linearly with the depths, which reached the minimum values when the depths were approximately $22.5m - NAP$, but the resistivities already started to decrease when the depth were approximately $23.5m - NAP$. This part of the slight hysteresis caused

the curve to experience a partial decline. If this area was excluded, the resistivity-water pressure head plots would not appear the resistivity decreasing parts. One reason could be that the resistivities at the dry and wet interface were not a constant value. The temperature changes, the solid conductivity and the concentration of the leachate were not taken into account.

Although the resistivities from ERT inversion are not the exact resistivity values in the waste body, it can represent the water content changing trends (Chavez Olalla *et al.*, 2021). The results verified that the relationships of resistivities and water pressure head were able to be matched by combining Archie's law and van Genuchten equation. Although the process to pick the suitable parameters was manual, the fitted curves managed to capture the cap of the curves using measured data, and the parameters indicated that the material in the waste body could be divided into several types, such as high porosity with high permeability material and low porosity with low permeability material. For this reason, the selection of resistivity being $20\Omega \cdot m$ can roughly provide a indication of where the waste body becomes wet or dry.

Table 7.1: Parameters that were used in the two equations to fit the correlations of measured resistivity and water pressure head values

	A $(-)$	ρ_w $(\Omega \cdot m)$	M $(-)$	N $(-)$	α (m^{-1})	n $(-)$	m $(-)$	S_{res} $(-)$	ϕ $(-)$
case 1.1	1	1.5	2.2	1.7	0.08	2.68	0.627	0.045	0.51
case 1.2	1.1	1.5	2.5	1.3	0.08	2.68	0.627	0.02	0.51
case 1.3	0.48	5	1.3	2	0.52	1.6	0.375	0.168	0.51
case 1.4	0.41	5	1.3	2	2.2	1.6	0.375	0.14	0.51
case 2.1	1	1.5	2.2	1.7	0.112	2.68	0.627	0.045	0.51
case 2.2	1.1	1.5	2.5	1.3	0.18	2.68	0.627	0.02	0.51
case 2.3	1.15	2	1.3	2	0.05	1.09	0.083	0.068	0.51
case 2.4	0.4	5	1.3	2	2.5	1.6	0.375	0.14	0.51
minimum	0.4	1.5	1.3	1.3	0.05	1.09	0.083	0.02	0.51
maximum	1.15	5	2.5	2	2.5	2.68	0.627	0.168	0.51

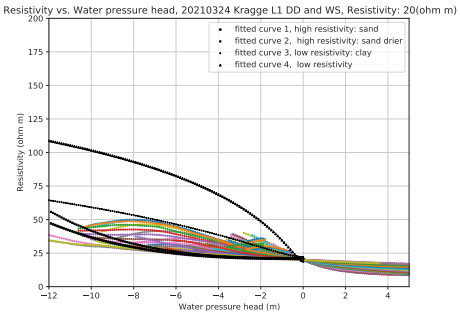

(a) Fit 1 Line 1 on 2021 March 24

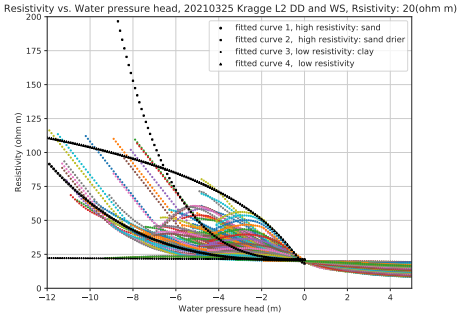

(b) Fit 2 Line 2 on 2021 March 25

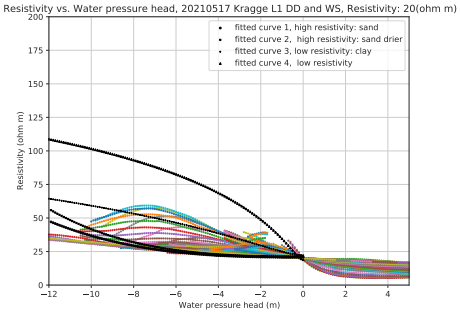

(c) Fit 1 Line 1 on 2021 May 17

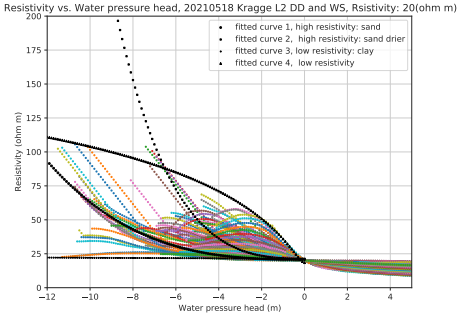

(d) Fit 2 Line 2 on 2021 May 18

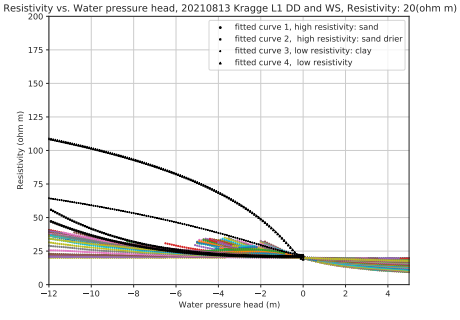

(e) Fit 1 Line 1 on 2021 August 13

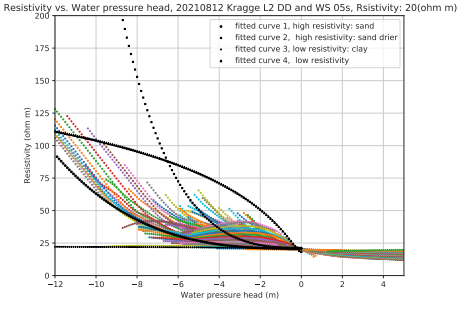

(f) Fit 2 Line 2 on 2021 August 12

Figure 7.12: Relationships of measured resistivities and water pressure head from ERT inversion grid maps and their fitted curves in Line 1 and Line 2.

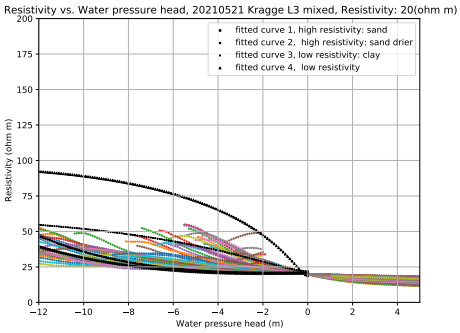

(a) Fit 1 Line 3 on 2021 May 21

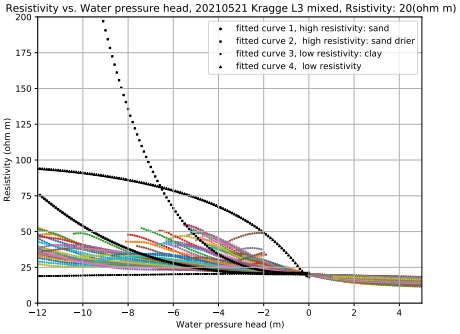

(b) Fit 2 Line 3 on 2021 May 21

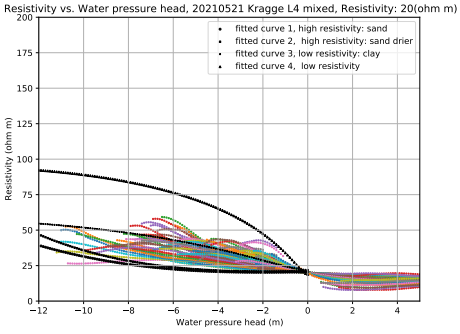

(c) Fit 1 Line 4 on 2021 May 21

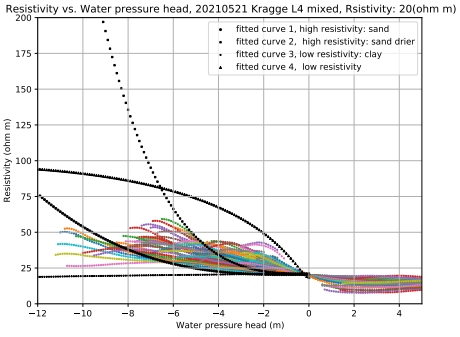

(d) Fit 2 Line 4 on 2021 May 21

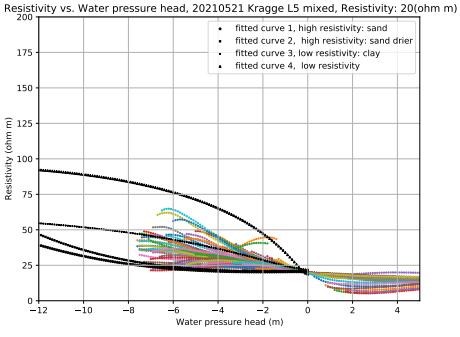

(e) Fit 1 Line 5 on 2021 May 21

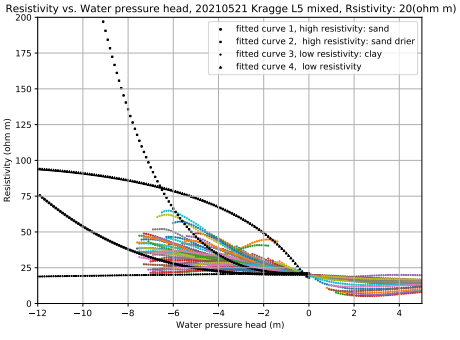

(f) Fit 2 Line 5on 2021 May 21

Figure 7.13: Relationships of measured resistivities and water pressure head from ERT inversion grid maps and their fitted curves in Line 3-5.

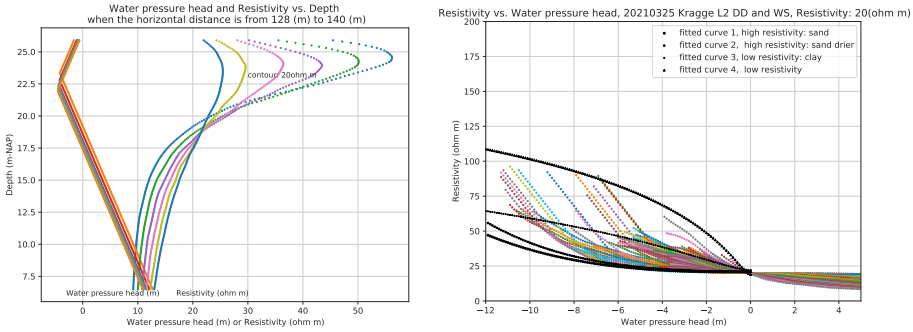

(a) Water pressure head or Resistivity vs. depth from the top wet area Line 2 on 2021 March 25

(b) Resistivity vs. water pressure head Line 2 on 2021 March 25

Figure 7.14: Measured and computed resistivity vs. water pressure head after removing the top wet area on Line 2.

8

Discussion

8.1. Regularization problems in ERT inversion

The regularization parameter 'λ' represents the degree of smoothness of the possible artifacts during inversion. In particular, the routes of the current followed 3D paths through the waste body, while the dimension was reduced to 2D when carrying out the ERT inversion. Besides, the increase of depth increased the uncertainty of the current direction, which led to larger errors at the bottom. Therefore, a smaller error corresponds to a larger regularization strength with larger 'λ' and vice versa.

The idea of regularization check is to search for resistivity pattern that matches best to the measurement values. Figure 8.1 shows the inversion results of Line 1 dipole-dipole array on 2021 March 24 when λ ranged from 1 to 100. 'λ = 100.0' looks over-smoothed and failed to fit the data appropriately, and the 'λ' between 1.0 and 10.0 may produce some unrealistic artifacts, for example, the low surface apparent resistivity plume where x coordinate is around 90m and 100m may come from too many reciprocal errors were deleted, which resulted in the insufficient data for inversion. There are many potential solutions that gave similar inversion plots, 'λ' between 10.0 and 30.0 could

all be a reasonable result, the idea of inversion is to find the parameter that gives the simplest solution, considering that most of the large errors had been removed before inversion, the final λ was chosen to be 20.0.

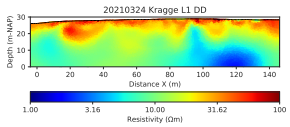

(a) Using 'λ = 1.0' to invert ERT results of Line 1 dipole-dipole array on 2021 March 24

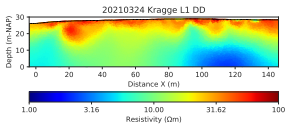

(b) Using 'λ = 5.0' to invert ERT results of Line 1 dipole-dipole array on 2021 March 24

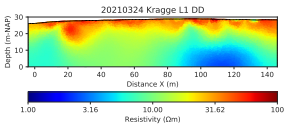

(c) Using 'λ = 10.0' to invert ERT results of Line 1 dipole-dipole array on 2021 March 24

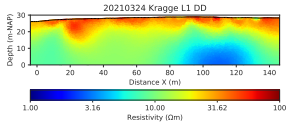

(d) Using 'λ = 20.0' to invert ERT results of Line 1 dipole-dipole array on 2021 March 24

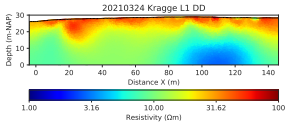

(e) Using 'λ = 30.0' to invert ERT results of Line 1 dipole-dipole array on 2021 March 24

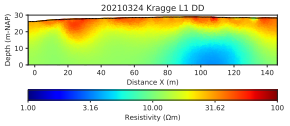

(f) Using 'λ = 100.0' to invert ERT results of Line 1 dipole-dipole array on 2021 March 24

Figure 8.1: Influence of regularization parameter 'λ' on ERT inversion results.

8.2. Sensitivity analysis of water retention curve parameters

When coupling the Archie's law and van Genuchten equation to form the water retention curve, there were 8 unknown parameters in total. The 'standard' parameters are listed in Table 8.1, and the results of only changing one parameter in each time are shown in Figure 8.2, and the Y-axes of the figures are expressed in logarithm scale.

We defined the starting point as when the water pressure head was $0m$. The similarity is that when the waste body became drier, the pressure head became more negative. Different parameters also have different effects on the changes of the curve trend. Parameter A and ρ_w show similar influence to the resistivity-water pressure head curves, making the curves shift upward, and the shift rate gradually decrease with the increase in these two parameters. The

influence of M on the curves is exponential. The sloop of the curve becomes steeper with the increase in M. When M is 2.8, the maximum resistivity can reach up to $7000\Omega \cdot m$. When N and ϕ increase uniformly, the curves also shift upward uniformly. The influence of the four parameters in the van Genuchten equation on the final curve is more complex, because the van Genuchten equation is more complicated. The changes of these parameters did not affect the resistivity value at the starting point. The increase of α, m and n all make the curves appear more significant growth in the first few meters, following by a platform in the following meters, while the increase of S_{res} makes the slope of the entire curves increase.

Table 8.1: Starting value of formula parameters

	Parameters	value
Archie's law	A	1.2
	ρ_w	$2.0\Omega \cdot m$
	M	1.3
	N	2.0
van Genuchten equation	α	1.5
	n	1.6
	m	0.375
	S_{res}	0.172

A balance of all the parameters need to be taken into consideration when fit the water retention curves, since the change of one parameter will result in different choices of all the other parameters. For example, in case 1.3, 1.4 and 2.4 (Table 7.1), the values of A were less than the commonly recommended value ranges, it is because the values of the leachate resistivity (ρ_w) were selected large than other cases. But this fitting process still has some limitations. Figure 8.2 shows that resistivity does have the potential to decrease with more negative water pressure heads in some cases, and the fitted curves failed to represent some measured features well at present. The influence of temperature was not included, while Glover (2016) pointed out that the resistivity of an aqueous pore fluid changes by about 2.3 $\%per^{\circ}C$ when the temperature is lower than $100^{\circ}C$. The temperature becomes higher with

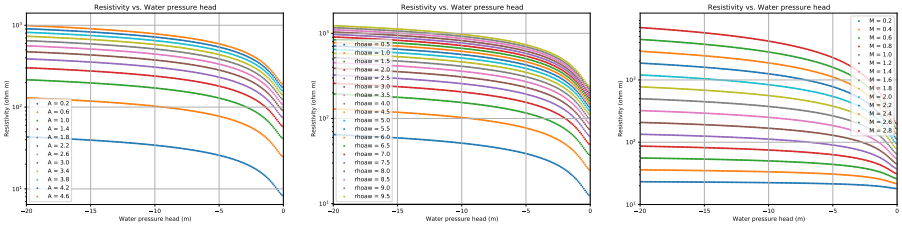

(a) Resistivity vs. water pressure head with changing parameter 'A' (b) Resistivity vs. water pressure head with changing parameter 'ρ_w' (c) Resistivity vs. water pressure head with changing parameter 'M'

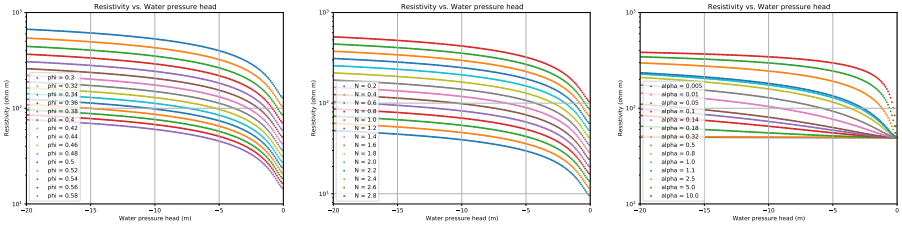

(d) Resistivity vs. water pressure head with changing parameter 'N' (e) Resistivity vs. water pressure head with changing parameter 'ϕ' (f) Resistivity vs. water pressure head with changing parameter 'α'

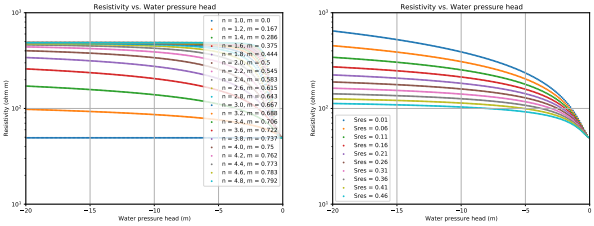

(g) Resistivity vs. water pressure head with changing parameter 'n' and 'm' (h) Resistivity vs. water pressure head with changing parameter 'S_{res}'

Figure 8.2: Influence of equation parameters on the relationship between resistivity and water pressure head.

the increase in depth, therefore, the resistivity of the waste body is higher under the same porosity and water content. Besides, those parameters were selected based on literature, the values may not be in line with the actual physical meaning.

8.3. Saturated area estimation

The saturated area (A_{sat}) was assumed to be within the contour lines that the resistivities are smaller than $20\Omega \cdot m$. The saturated content (θ_w) was take to be 0.58, assuming that the longitudinal measurement influence range (y direction) was $1m$, then the saturated volume (V_{sat}) was calculated by:

$$V_{sat} = 1 \times \theta_w \cdot A_{sat} \tag{8.1}$$

The results are shown in Table 8.2 and Figure 8.3. It can be seen that the volume of saturated water kept almost unchanged during these 5 months, with only a small amount of dryness in the summer, which could be understood as a result of strong evaporation. Other analysis also indicated that the water level in the drainage system remained the same in the long term, therefore, it seems that the input water source, such as infiltration and rainfall, were flowing preferentially through large vertical gap without being stored in the waste body.

Table 8.2: Estimation of saturated area and volume from resistivity contour.

Date & Line (-)	Saturated area (m^2)	Saturated volumn (m^3)
2021 March 24 L1	297.92	172.79
2021 March 25 L2	282	163.56
2021 May 17 L1	288.95	167.59
2021 May 18 L2	275.99	160.07
2021 May 21 L3	134.87	78.22
2021 May 21 L4	199.64	115.79
2021 May 21 L5	207.55	120.38
2021 August 12 L2	287.67	166.85
2021 August 13 L1	270.16	156.69

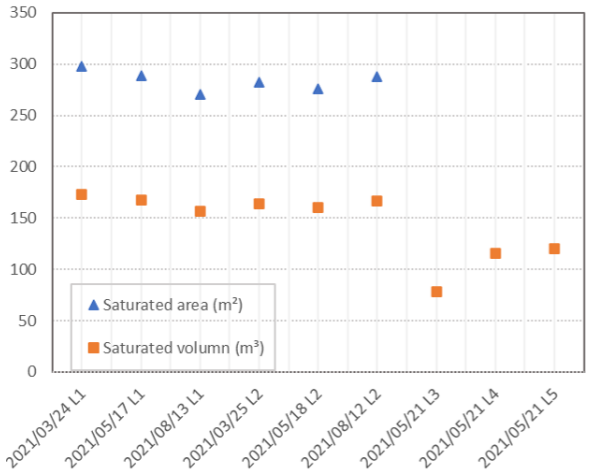

Figure 8.3: Estimation of saturated area and volume from resistivity contour.

9

Conclusions

9.1. Research question validation

In conclusion, this research presents the application of electrical resistivity tomography (ERT) to visualize the water distribution in the landfill. Five ERT lines were set up and measured at different dates. GPS measurement were conducted to provide 3D coordinates of the electrodes and wells. The measurement error was assessed to make the ERT data more stable and robust. The electrical resistivity measurement gives most accurate results near the surface. The resistivity values decrease dramatically with the increase in the saturation of leachate. The results show that electrical resistivity inversion maps are able to visualize the water distribution pattern in the landfill waste body. The maps clearly delineate the depth and lateral extension of the top water table, which shows significant gradient variations. There also exists some wet bulks above the dry surface as well as dry bulks below the wet zones, which form the local ponding, and there are low-permeability waste barriers that hinder the free diffusion of water. As a results, the ERT results fail to explain the water level measured in the wells, since the water levels in the wells can only represent the water pressure heads at the filters at the bottom

of the wells.

Laplacian edge detection cannot depict the interface of the dry and wet areas in the waste body. It is because of the high heterogeneity in the waste body while this technique is more sensitive to the anisotropic layers. By using Archie's law and van Genuchten equation, the relations between the resistivities and water pressure heads can be modelled. The fitted curves indicate that the material in the waste body is quite heterogeneous, and several properties can be recognized, such as high porosity with high permeability material and low porosity with low permeability material. These analysis results along with the observations from the resistivity inversion maps verify the existence of preferential flow in the waste body. Time-lapse measurements show that the temporal changes of the landfill are extremely limited. Quantitative estimation of the saturated water volumes of the measurement areas indicates that the waste body becomes moderately drier in summer, which may be owing to the fact that the increase in temperature accelerates the evaporation effect, so the hypothesis of the hydrostatic condition is valid.

9.2. Recommendations

The conclusions are specific for the landfill Kragge (cell 3). In the current stage, there are several limitations of this research: (a) the sources of error have not been clearly identified; (b) the ERT inversion results have not been able to be connected to the field situations as well as the water balance model; (c) the parameters water retention curve analysis were chosen based on the former experience.

Another limitation is from the inversion process, although the electrical resistivity measurements are precise, the regularization parameter have a great influence on the smoothness of the graph and can affect the accuracy of the inversion results. Accordingly, using the certain value of $20\Omega \cdot m$ to distinguish the wet-dry boundaries is a great risk. In addition, the influence of the variations of temperature and porosity on the resistivities of waste body is not considered.

These limitations persuaded us to go back to the field again to better

explore the situation of the landfill. So the future work can focus more on comparing the ERT maps with the field conditions, such as infiltration systems, bottom liner positions as well as rainfall situations. More wells can be drilled along the ERT lines to have further verification of the water level. The laboratory work is also interested to quantify the resistivity-waste water content relations.

Besides, 3D inversion of ERT results are also suggested, in order to make use of the three horizontal lines, to better illustrate the water distributions within relative close areas.

Bibliography

K. Knödel, H. Krummel, and G. Lange, *Handbuch zur Erkundung des Untergrundes von Deponien und Altlasten: Band 3: Geophysik* (Springer-Verlag, 1997).

I. Wiekenkamp, *Possibilities and limitations of using global search algorithms for Electrical Resistivity Tomography (ERT) inversion*, Ph.D. thesis (2012).

T. Dahlin and B. Zhou, *A numerical comparison of 2d resistivity imaging with 10 electrode arrays,* Geophysical prospecting **52**, 379 (2004).

J. Rodrigo-Ilarri, M.-E. Rodrigo-Clavero, and E. Cassiraga, *Bioleach: A new decision support model for the real-time management of municipal solid waste bioreactor landfills,* International journal of environmental research and public health **17**, 1675 (2020).

P. Kjeldsen, M. A. Barlaz, A. P. Rooker, A. Baun, A. Ledin, and T. H. Christensen, *Present and long-term composition of msw landfill leachate: a review,* Critical reviews in environmental science and technology **32**, 297 (2002).

W. Kattenberg and T. Heimovaara, *Policy process of allowing research pilots for sustainable emission reduction at landfills in the netherlands,* in *Proceedings Sardinia* (2011).

P. R. Schroeder, T. S. Dozier, P. A. Zappi, B. M. McEnroe, J. W. Sjostrom, R. L. Peyton, *et al.*, *The hydrologic evaluation of landfill performance (help) model: Engineering documentation for version 3,* (1994).

J. Fellner and P. H. Brunner, *Modeling of leachate generation from msw landfills by a 2-dimensional 2-domain approach,* Waste Management **30**, 2084 (2010).

J. Fellner, *A new method for modeling water flow and water storage in municipal solid waste landfills*, Ph.D. thesis (2004).

H. Rosqvist and D. Bendz, *An experimental evaluation of the solute transport volume in biodegraded municipal solid waste,* Hydrology and earth system sciences **3**, 429 (1999).

N. Rosqvist, L. Dollar, and A. Fourie, *Preferential flow in municipal solid waste and implications for long-term leachate quality: valuation of laboratory-scale experiments,* Waste management & research **23**, 367 (2005).

A. van Turnhout, *Characterizing dominant processes in landfills to quantify the emission potential,* (2017).

M. Hrachowitz, P. Benettin, B. M. Van Breukelen, O. Fovet, N. J. Howden, L. Ruiz, Y. Van Der Velde, and A. J. Wade, *Transit times—the link between hydrology and water quality at the catchment scale,* Wiley Interdisciplinary Reviews: Water **3**, 629 (2016).

A. Zacharof and A. Butler, *Stochastic modelling of landfill leachate and biogas production incorporating waste heterogeneity. model formulation and uncertainty analysis,* Waste management **24**, 453 (2004).

T. Heimovaara, A. Bun, and A. Van Turnhout, *Water balance modeling for estimation of residence time of water in a full-scale landfill using a data-assimilation approach,* in *HPM6: The 6th International Workshop Hydro-Physico-Mechanics of Landfills, Delft, The Netherlands, 14-17 April 2015* (Citeseer, 2015).

A. G. van Turnhout, C. Brandstätter, R. Kleerebezem, J. Fellner, and T. J. Heimovaara, *Theoretical analysis of municipal solid waste treatment by leachate recirculation under anaerobic and aerobic conditions,* Waste Management **71**, 246 (2018).

A. Setianto and T. Triandini, *Comparison of kriging and inverse distance weighted (idw) interpolation methods in lineament extraction and analysis,* Journal of Applied Geology **5** (2013).

B. Zhou and I. Kanl, *Electrical resistivity tomography: a subsurface-imaging technique,* in *Applied geophysics with case studies on environmental, exploration and engineering geophysics* (IntechOpen London, UK, 2018).

P. Brunet, R. Clément, and C. Bouvier, *Monitoring soil water content and deficit using electrical resistivity tomography (ert)–a case study in the cevennes area, france,* Journal of Hydrology **380**, 146 (2010).

A. Neyamadpour, *3d monitoring of volumetric water content using electrical resistivity tomography in municipal solid waste landfill,* Environmental Earth Sciences **78**, 1 (2019).

G. C. Topp, J. Davis, and A. P. Annan, *Electromagnetic determination of soil water content: Measurements in coaxial transmission lines,* Water resources research **16**, 574 (1980).

O. Kuras, J. D. Pritchard, P. I. Meldrum, J. E. Chambers, P. B. Wilkinson, R. D. Ogilvy, and G. P. Wealthall, *Monitoring hydraulic processes with automated time-lapse electrical resistivity tomography (alert),* Comptes Rendus Geoscience **341**, 868 (2009).

R. Clément, M. Descloitres, T. Günther, L. Oxarango, C. Morra, J.-P. Laurent, and J.-P. Gourc, *Improvement of electrical resistivity tomography for leachate injection monitoring,* Waste management **30**, 452 (2010).

M. Chrétien, J. Lataste, R. Fabre, and A. Denis, *Electrical resistivity tomography to understand clay behavior during seasonal water content variations,* Engineering geology **169**, 112 (2014).

G. E. Archie, *The electrical resistivity log as an aid in determining some reservoir characteristics,* Transactions of the AIME **146**, 54 (1942).

M. Audebert, L. Oxarango, C. Duquennoi, N. Touze-Foltz, N. Forquet, and R. Clément, *Understanding leachate flow in municipal solid waste landfills by combining time-lapse ert and subsurface flow modelling–part ii: Constraint methodology of hydrodynamic models,* Waste management **55**, 176 (2016).

S. M. de Jong, R. A. Heijenk, W. Nijland, and M. van der Meijde, *Monitoring soil moisture dynamics using electrical resistivity tomography under homogeneous field conditions,* Sensors **20**, 5313 (2020).

M. Audebert, R. Clément, N. Touze-Foltz, T. Günther, S. Moreau, and C. Duquennoi, *Time-lapse ert interpretation methodology for leachate injection monitoring based on multiple inversions and a clustering strategy (mics),* Journal of Applied Geophysics **111**, 320 (2014).

R. Clément, L. Oxarango, and M. Descloitres, *Contribution of 3-d time-lapse ert to the study of leachate recirculation in a landfill,* Waste management **31**, 457 (2011).

J. Rings, A. Scheuermann, K. Preko, and C. Hauck, *Soil water content monitoring on a dike model using electrical resistivity tomography,* Near Surface Geophysics **6**, 123 (2008).

J. Chavez Olalla, *Electrical Resistivity Tomography Protocol for Landfill Monitoring*, Master's thesis (2017).

S. Grellier, K. Reddy, J. Gangathulasi, R. Adib, and C. Peters, *Correlation between electrical resistivity and moisture content of municipal solid waste in bioreactor landfill,* in *Geoenvironmental Engineering* (2007) pp. 1–14.

H.-L. Hsu, B. J. Yanites, C.-c. Chen, and Y.-G. Chen, *Bedrock detection using 2d electrical resistivity imaging along the peikang river, central taiwan,* Geomorphology **114**, 406 (2010).

J. Chambers, P. Wilkinson, D. Wardrop, A. Hameed, I. Hill, C. Jeffrey, M. Loke, P. Meldrum, O. Kuras, M. Cave, *et al.*, *Bedrock detection beneath river terrace deposits using three-dimensional electrical resistivity tomography,* Geomorphology **177**, 17 (2012).

J. Chavez Olalla, T. Winkels, D. Ngan-Tillard, and T. Heimovaara, *Geophysical tomography as a tool to estimate the geometry of soil layers: relevance for the reliability assessment of dikes,* Georisk: Assessment and Management of Risk for Engineered Systems and Geohazards , 1 (2021).

A. Samouëlian, I. Cousin, A. Tabbagh, A. Bruand, and G. Richard, *Electrical resistivity survey in soil science: a review,* Soil and Tillage research **83**, 173 (2005).

A. Dey and H. Morrison, *Resistivity modelling for arbitrarily shaped two-dimensional structures,* Geophysical Prospecting **27**, 106 (1979).

M. H. Loke, *Tutorial: 2-d and 3-d electrical imaging surveys,* (2013).

M. Hanke, B. Harrach, and N. Hyvönen, *Justification of point electrode models in electrical impedance tomography,* Mathematical Models and Methods in Applied Sciences **21**, 1395 (2011).

T. Günther, C. Rücker, and K. Spitzer, *Three-dimensional modelling and inversion of dc resistivity data incorporating topography—ii. inversion,* Geophysical Journal International **166**, 506 (2006).

A. Furman, T. P. Ferré, and A. Warrick, *A sensitivity analysis of electrical resistivity tomography array types using analytical element modeling,* Vadose Zone Journal **2**, 416 (2003).

B. Zhou and T. Dahlin, *Properties and effects of measurement errors on 2d resistivity imaging surveying,* Near surface geophysics **1**, 105 (2003).

S. Korteland, *Quantitative characterization of solute transport processes in the laboratory using electrical resistivity tomography,* (2013).

S.-A. Korteland and T. Heimovaara, *Quantitative inverse modelling of a cylindrical object in the laboratory using ert: An error analysis,* Journal of Applied Geophysics **114**, 101 (2015).

C. Rücker, *Advanced electrical resistivity modelling and inversion using unstructured discretization*, Ph.D. thesis, Universität Leipzig (2010).

T. Günther and C. Rücker, *Boundless electrical resistivity tomography bert 2–the user tutorial,* (2013).

C. Rücker, T. Günther, and F. M. Wagner, *pyGIMLi: An open-source library for modelling and inversion in geophysics,* Computers and Geosciences **109**, 106 (2017).

C. Rücker, T. Günther, and K. Spitzer, *Three-dimensional modelling and inversion of dc resistivity data incorporating topography—i. modelling,* Geophysical Journal International **166**, 495 (2006).

P. Virtanen, R. Gommers, T. E. Oliphant, M. Haberland, T. Reddy, D. Cournapeau, E. Burovski, P. Peterson, W. Weckesser, J. Bright, S. J. van der Walt, M. Brett, J. Wilson, K. J. Millman, N. Mayorov, A. R. J. Nelson, E. Jones, R. Kern, E. Larson, C. J. Carey, İ. Polat, Y. Feng, E. W. Moore, J. VanderPlas, D. Laxalde, J. Perktold, R. Cimrman, I. Henriksen, E. A. Quintero, C. R. Harris, A. M. Archibald, A. H. Ribeiro, F. Pedregosa, P. van Mulbregt, and SciPy 1.0 Contributors, *SciPy 1.0: Fundamental Algorithms for Scientific Computing in Python,* Nature Methods **17**, 261 (2020).

M. T. Van Genuchten, *A closed-form equation for predicting the hydraulic conductivity of unsaturated soils,* Soil science society of America journal **44**, 892 (1980).

P. O. Falae, D. P. Kanungo, P. K. S. Chauhan, and R. K. Dash, *Electrical resistivity tomography (ert) based subsurface characterisation of pakhi landslide, garhwal himalayas, india,* Environmental Earth Sciences **78**, 1 (2019).

P. W. Glover, *Archie's law–a reappraisal,* Solid Earth **7**, 1157 (2016).

M. Ibarra Gonzalez, *10 channels resistivity-meter for resistivity and chargeability measurements user's manual,* (2018).

A

Syscal Protocol

The Syscal protocol includes the steps to deign experiments, set machine parameters and acquire the results. The parameter setting steps was written based on Ibarra Gonzalez (2018), but it is more specific for the ERT measurement in the landfill Kragge.

Protocol of Using Syscal Pro to Do ERT Surveys

18/02/2021 Zhenlu Ren

Contents

A1. Summary of the steps:

1. Before field work:
    1.1 Planning the measurement area, date, people, etc.
    1.2 Determining the array
    1.3 Collecting the instruments
    1.4 Generating the sequence files on the laptop
    1.5 Passing the data to the Syscal Pro unit
2. During field work:
    2.1 Installing the electrodes on the field
    2.2 setting up the procedure
    2.3 Opening the machine and battery to start the measurements
    2.4 Combined with GPS measurement, TDR measurement, Diver measurement, etc.
3. After field work:
    3.1 Passing the results back to laptop
    3.2 Viewing the results
    3.3 Doing inversion

A2. Planning the measurement area

This protocol will take the ERT survey in the landfill Kragge for example.

A2.1. Reason

The aim is to test if we can use an ERT survey to map the distribution in water table in the waste body. The number of wells is small relative to the total surface area of the landfill cell, so the spatial distribution of the water table is difficult to interpolate.

This protocol gives every step in order to finish a ERT survey. It will give instructions to other Syscal Pro users.

A2.2. Area

The choice of the experimental site needs to be based on the interpretation of previous ERT results as well as the current water level data measured in the monitoring wells.

It is very interesting to know how the water (leachate) level varies between two adjacent wells which show large differences in water table. The new ERT lines will be positioned where we expect large variations in space.

The new measurements can be carried out on: (i) the old ERT lines, (ii) the extension lines on the original lines, (iii) polyline between some wells, (iv) etc.

- **Example of ERT lines**

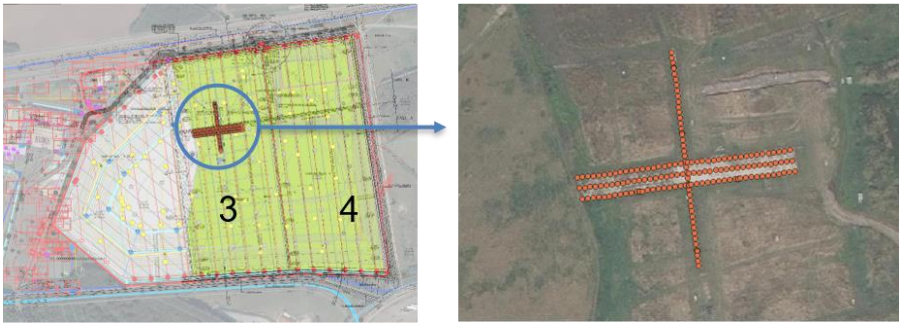

Figure 1. Top view of Kragge and old ERT lines

A2.3. Dates

Considering the number of electrodes and selection of arrays, one measurement will take 2-3 h after pressuring the "start". For each measurement line, a reciprocal array is needed so the total time will be double.

The time for extra measurement such as GPS measurement should also be considered.

3-5 people is needed every time.

Setting up the instruments may take 3-4 h, it is better to be finished before going to the field.

After attaining good results, measurements can be done regularly (namely time-lapse ERT).

A3. Determining the array

A3.1. Principle

http://www.iris-instruments.com/Pdf_file/Resistivity_Sounding/summary_of_operation.pdf

http://personales.upv.es/jpadin/coursenotes.pdf

1. (Wenner-)Schlumberger array:

   It is sensitive to vertical changes in the subsurface resistivity below the center of the array. But it is less sensitive to horizontal changes in the subsurface area. Therefore, Wenner array is good in resolving vertical changes (horizontal structures (soil layers)), but relatively poor in detecting horizontal changes (narrow vertical structures). The geometric factor for the Wenner array is 2πa, the median depth of investigation for the Wenner Alpha array is about 0.5a. The Wenner array has the strongest signal strength, to resist high background noise.

2. Dipole-dipole array:

   It is sensitive to horizontal changes in resistivity, but relatively insensitive to vertical changes in the resistivity. That means it is good in mapping vertical structures but relatively poor in mapping horizontal structures. The disadvantage is the very small signal strength for large values of the 'n' factor.

Choose an appropriate array and do the reciprocal one. The reciprocal array uses the same sequence as the original one, but it converts the pair of electrodes that originally input current to receive voltage, and the pair of electrodes that originally receive voltage to input current. The original and reciprocal resistivity maps should be the same or at least similar, which indicates that it is possible to use the selected array.

A4. Collecting the instruments

http://www.iris-instruments.com/syscal-pro.html

http://www.iris-instruments.com/Checklists/checklist_Syscal_standard.pdf

http://www.iris-instruments.com/Pdf_file/Accessories_RhoIP.pdf

The Syscal Pro gathers a 10 channels receiver and a 250W, 2000Vpp internal transmitter which make it the more powerful system of the Syscal range. This system allows to perform up to 10 measurements at a time and its switching board allow to work for 48 (Switch-48) up to 120 (Switch-120) electrodes. (From Syscal website)

- Syscal Pro units (main & extension):
- Two black batteries per box per day. The batteries are needed for the main box

and for the extension box (black battery)

- Battery chargers for black batteries
- Connection cable battery to box (alligator connection at one end pin at the other)
- Orange connection cables (18 or 36 connections). The 18-connection cables have to be connected to make a 36-connection cable
- Alligator clips (thin-orange cable with two alligator clips at both ends)
- Electrodes (metals pints) (max=216 for machine)
- Field work laptop with software and data needed
- Connection cable between laptop and main box (data upload and download)
- Charger
- Generator
- Hammer
- Measuring tapes
- Wheelbarrow or similar
- Tent
- Security pack
- Own laptop

Notes:

- Most things are in one of the blue boxes
- Charge the main and the extension box the night before
- Charge the batteries
- Charge the laptop
- Prepare file beforehand
- Upload the file
- You can always take some extra materials (cables, batteries, etc)

Other stuff:

- GPS system.
- Safety shoes, clothes, helmets, gloves, masks.
- Protocol & manuals & plans & reports.
- Notebooks, recording tables, pens, etc.
- Long wooden stakes, labels, yellow warning sign, connector protection cover, Construction warning tape.
- Printed maps.
- Lunch.


wooden stakes


Construction warning tapes


Wheelbarrow


Measuring taps


Shovel


Hammer


Field work laptop & data connection cable


Syscal green box


Syscal pro screen


Syscal pro body


Syscal pro body


Electrodes and cables connected by alligator clips


Alligator clips for batteries


Orange cables


Alligator clips for electrodes


Electrodes

A5. Generating the sequence files on the laptop

1. Define the array types. For example:

   - dipole-dipole: good for 'vertical' structures

   - schlumberger and wenner: good for 'horizontal' structures

2. Use the Python scripts to generate the sequence file. The file should include the electrodes coordinates (do not need the true gps) and measuring arrays:

   https://github.com/jfchavezolalla/ERT_toolbox_CURE

3. Import and view the generated sequence file in the software **Electre Pro**.

http://www.iris-instruments.com/Pdf_file/ElectrePro_gb.pdf

The steps to operate the software are following:

- File >> open
- Create standard seq.

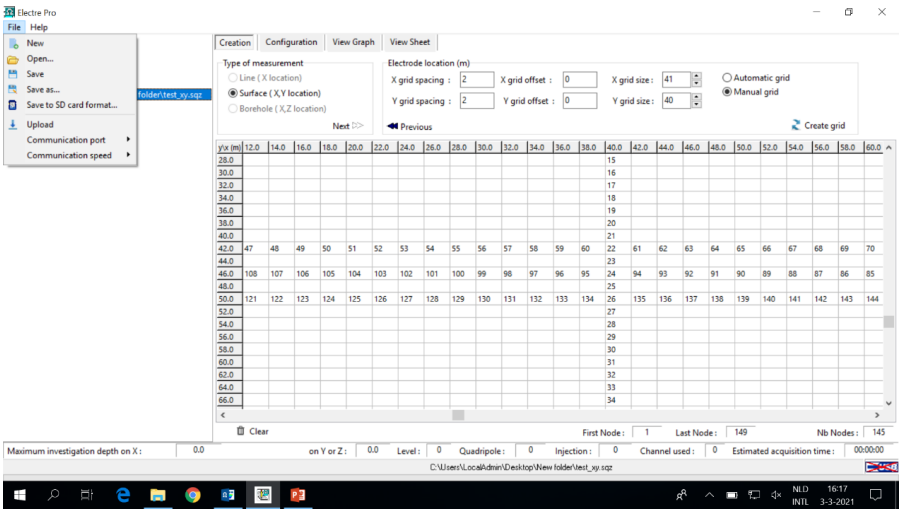

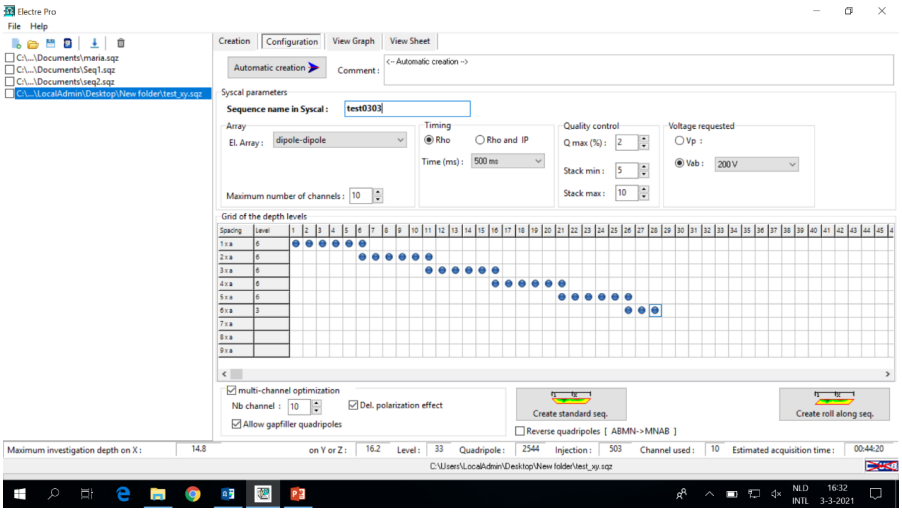

A6. Passing the data to the Syscal Pro unit

Click the 'upload' button in the software **Electre Pro.** Open the machine. Use the button "upload" and pressure "upload from pc" to transmit the data from laptop to machine. Remember the memory number and the file name on the laptop and select the right one on the machine.

- File >> upload

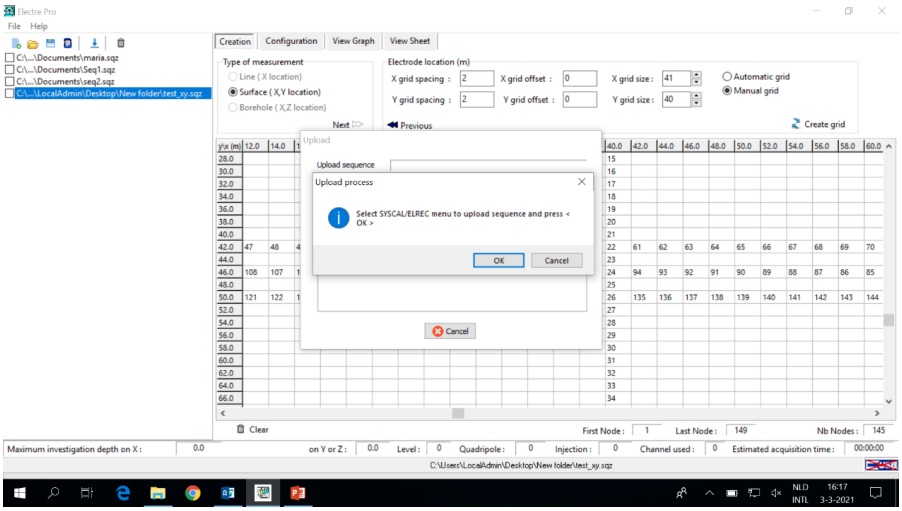

A7. Installing the electrodes on the field

1. In the case shown in the figure below, the 18 electrodes are installed every 0.5m with a total length of 9m. The position of ERT lines and electrodes should be measured with measuring taps and GPS.
2. The electrodes are fixed in the ground by hammers. Make sure the electrodes have good contact with soil and cannot be shaken.
3. Use cord clips to link electrodes to the corresponding connection points on the orange cables.
4. Switch on the machine and set up the parameters. (Refer to part 7)
5. Then connect the orange cables to the Syscal pro unit. Remember the number of electrodes.
6. Connect the machine to the external batteries with the black-and-red battery cables and start checking machine and measuring.

A8. setting up the procedure

Set up the parameters on the machine before connecting the cables to the Syscal machine.

A8.1. Config | Mode

In the menu 'Config | Mode', change the mode to 'automatic sequence'.

Automatic sequence can automatically switch the electrodes according to a preset sequence of measurement. This mode requires the use of a switching system.

(Press enter to continue the settings).

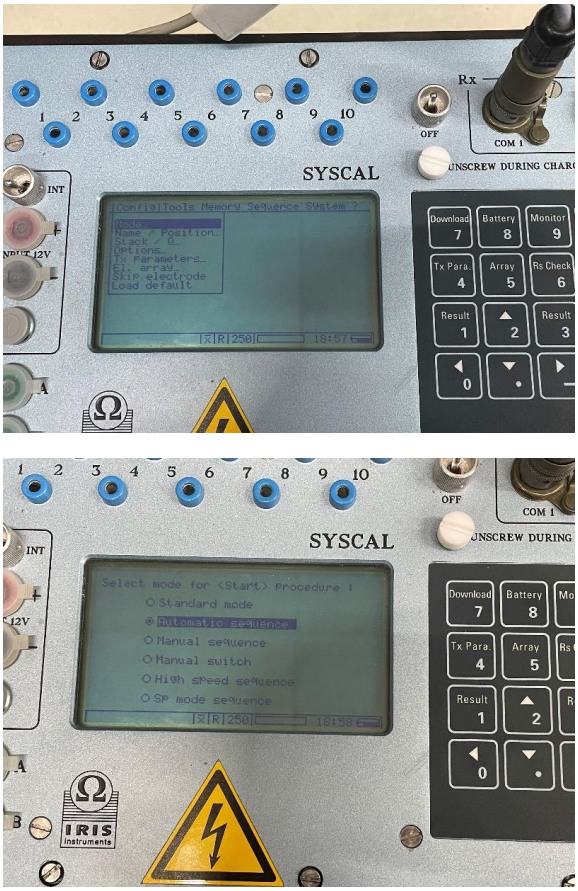

A8.2. Config | Name / Position

Use the same file name saved in the laptop.

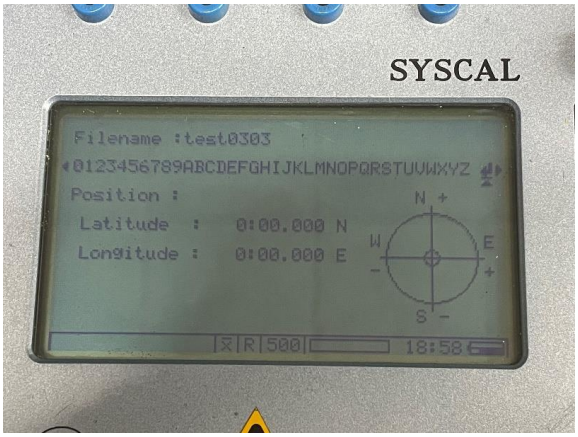

A8.3. Config | Stack/Q

1. Stacks min=5, max=10.

   Stack min / max is the minimum / maximum number of stacks (cycles) to do.

2. Qmax=2.

   It is the quality factor requested (standard deviation in %).

   As long as the quality factor is greater than the introduced value, the measurement will run up to the specified stack max. If not, it will stop to the stack min.

   The quality factor is computed for each channel but is checked relatively to the results obtained on the triggering channel.

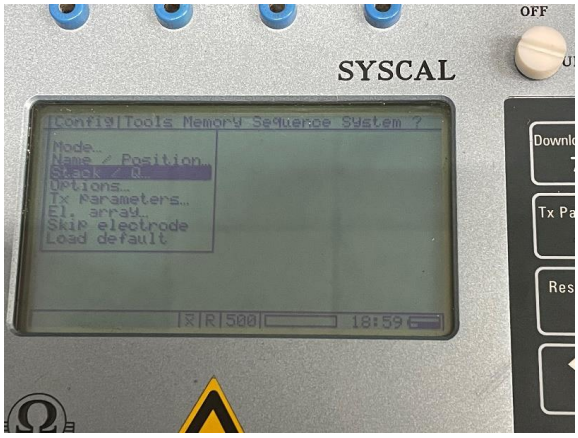

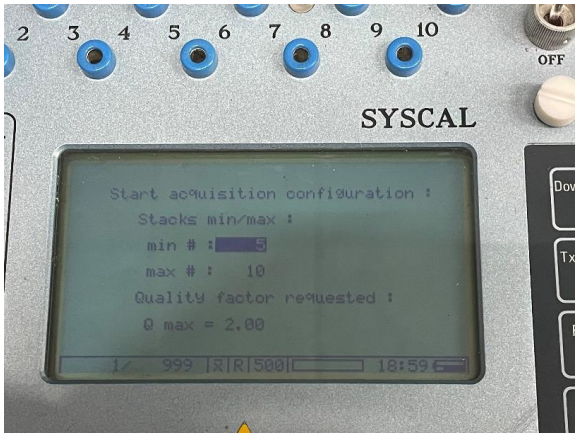

A8.4. Config | Options

1. Reading: average (X)

   'Average (X)' means that the displayed values will be the average values of the pulses from the beginning of the measurement.

2. Voltage: signed

   'Signed' means that the voltage values will have assign, which depends on the polarity of the measured dipole voltage with respect to the first dipole voltage. Consequently, the resistivity values will be also signed.

3. IP values: default.

   (We don't need to do IP measurement now.)

4. Spacing unit: meter

   The spacing values will be given in meters (standard).

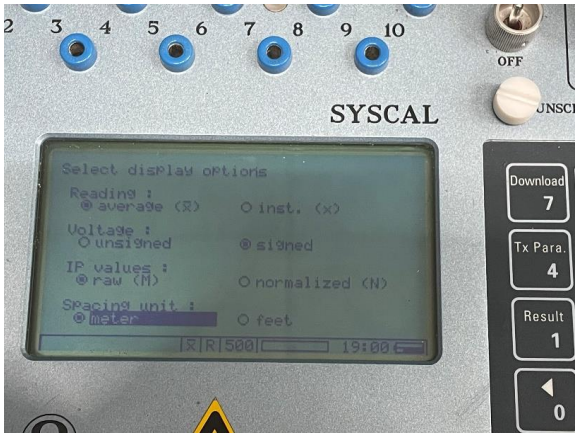

A8.5. Config | Tx parameters

1. Rho: Choose the 'Rho' measurement, which means resistivity only measurement.
2. Time: 500 msec. It is the injection pulse duration.
3. Vab requested: 'V | Iab'. Select a constant injection value of '200V'.

*Note: Current depends on the ground resistance (depend on the shape of the ground ohm's law).

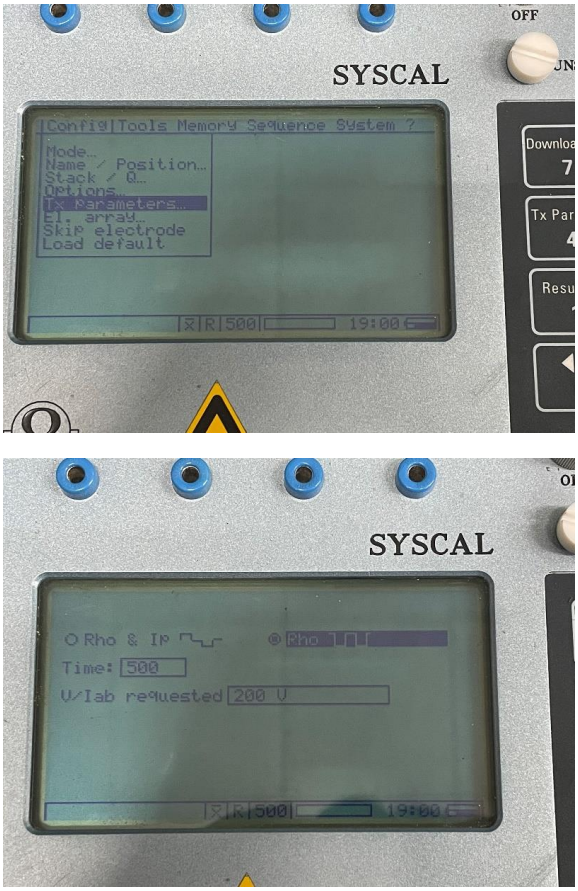

A8.6. Config | E.array

1. Select the array that used, for example, dipole-dipole.
2. Nb channel: 10 (which is the maximum channel of the machine).

A9. Start the measurement

1. Make sure a good connection between electrodes and the orange cables through cord clips; a good connection between the orange cables and the machine; and a good connection between the machine and the battery through battery cables.
2. Select and switch to the external battery on the machine.
3. Press the start button, then the machine checks the connections according to the measured ground resistance before the start. If Q (present) > Q (quality factor requested=2), which means the line is open, then we need to check the electrodes again.
4. 'Enter memory block. Store data from # 0-????' option: Remember to record the number of data that the storage should begin. This number is important when process the data on laptop. It can be viewed later using "export" option on the machine in case we forget.
5. Press the 'START' key. Then the measurements will automatically begin.
6. Repeat the steps for other measurements.
7. After finishing the measurements. Mark the measurement points on the field. Clean the site and collect and bring back all the instruments.

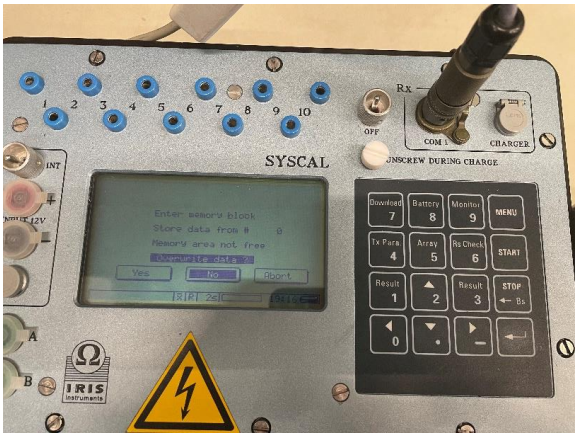
SYSCAL
Rx
OFF
COM 1
CHARGER
UNSCREW DURING CHARGE
Enter memory block
Store data from 0 0
Memory area not free
Overwrite data ?
Yes
No
Abort
Download 7
Battery 8
Monitor 9
MENU
Tx Para 4
Array 5
Rs Check 6
START
Result 1
Result 3
STOP
IRIS
Instruments


SYSCAL
Rx
OFF
COM 1
line resistance check
Enter to skip
Download 7
Battery 8
Monitor 9
Tx Para 4
Array 5
Result 1
IRIS

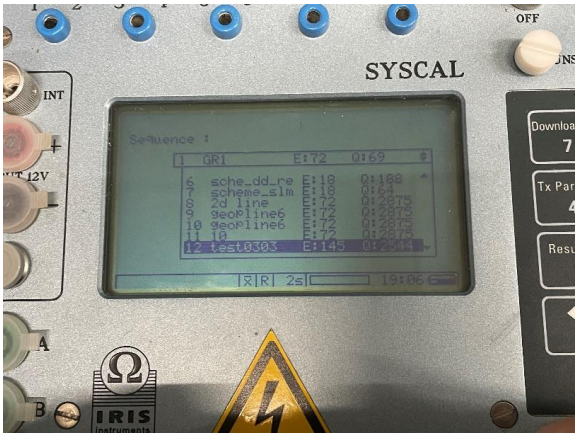
SYSCAL
OFF
Sequence :
1 GR1 E:72 0:69
6 sche_dd_re E:18 0:188
7 scheme_slm E:18 0:69
8 2d line E:72 0:2875
9 geoline6 E:72 0:2875
10 geoline6 E:72 0:2875
11 10 E:72 0:2875
12 test030% E:145 0:2874
IRIS
Instruments

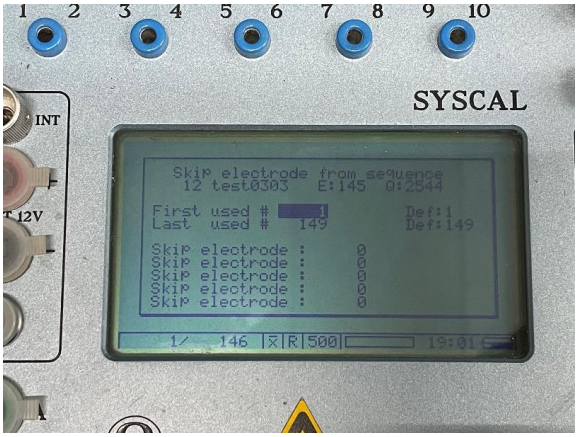

A10. Passing the results back to laptop

Download the data from the machine to laptop (memory → data download). Press the download button on the machine and import the data to the laptop. The results are stored in .bin file.

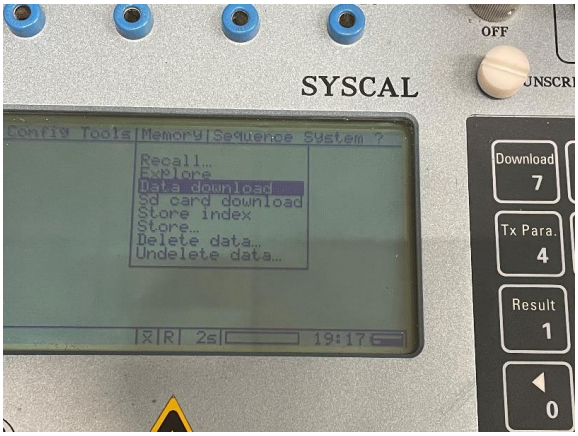

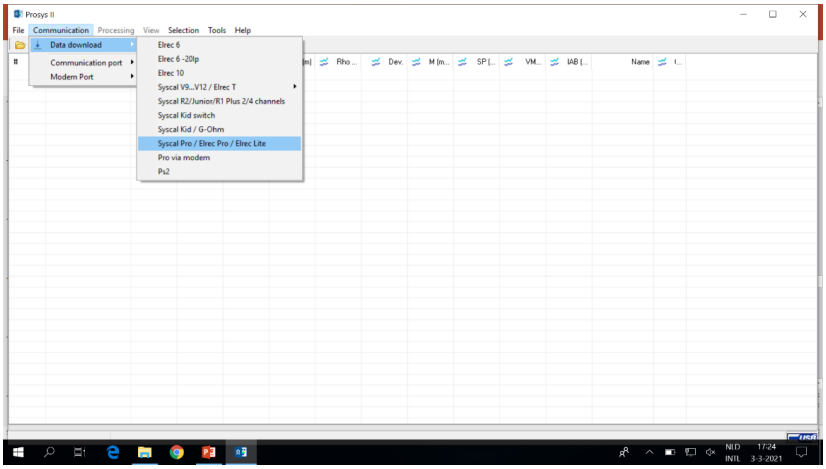

A11. Viewing the results

1. Interpolate the .bin files to .txt files: Done in Python.
2. Doing inversion and further analysis: Done in Python.